Movement and Force Measurement Systems as a Foundation for Biomimetic Research on Insects

---

A thesis submitted in partial fulfilment
of the requirements for the Degree of

Master of Engineering, in
Electrical & Electronic Engineering

at the University of Canterbury.

---

by C. H. Mills, B.E. Hons

University of Canterbury,
Christchurch, New Zealand.

June 2009.

Abstract

During the undertaken research and development, two major systems were designed. These were; a prototype force sensor, and a movement measurement system. Both the developed systems were designed for the intended field of insect research, but were developed using very different underlying principles. The force measurment system uses the piezo-electric effect induced in piezo-electric bimorph elements to produce a measure of force excerted on the sensor. The movement measurement system on the other hand uses computer vision (CV) techniques to find and track the three dimensional (3D) position of markers on the insect, and thereby record the pose of the insect.

To further increase the usefulness of the two measurement systems, a prototype graphical user interface (GUI) was produced to encapsulate the functionality of the systems and provide an end user with a more complete and functional research tool. The GUI allows a user to easily define the parameters required for the CV operations and presents the results of these operations to the user in an easily understood visual format. The GUI is also intended to display force measurements in a graphical means to make them easily interpreted. The GUI has been named Weta Evaluation Tracking and Analysis (WETA).

Testing on the developed prototype force sensor shows that the piezo-electric bimorph elements provide an adequate measure of force excerted on them, when the voltage signal produced by an element is integrated. Furthermore, the testing showed that the developed force sensor layout produces an adequate measure of forces in the two horizontal linear degrees of freedom (DOF), but the prototype did not produce a good measure of forces in the vertical linear DOF.

Development and testing of the movement measurement system showed that stereo vision techniques have the ability to produce accurate measurements of 3D position using two cameras. Although, when testing these techniques with one of the cameras replaced by a mirror, the system produced less than satisfactory results. Further testing on the feature detection and tracking portions of the movement system showed that even though thesesystems were implemented in a relatively simple way, they were still adequate in their associated operations. However, it was found that with some simple changes in colour spaces used during feature detection, the performance of the feature detection system in varyin illumination was greatly improved. The tracking system on the other hand, operated adequately using just its associated basic principles.

During the development of both prototype measurement systems, a number of conclusions were formulated that indicated areas of future development. These areas include; advanced force sensor configurations, force sensor miniturisation, design of a force plate, improvement of feature detection and tracking, and refining of the stereo vision equipment.

Acknowledgements

Firstly, thanks to Associate Professor Larry Field for providing sight for the project from a biology view point. Larry's past work on Weta and his input on how future studies could be conducted was very valuable.

Thanks to Paul Gaynor, without whom this research would not have been completed. As supervisor, Pauls constant input and support was a major driving force behind the research.

Additionally the author would like to extend thanks to the technicians and other staff in the Electrical and Computer Engineering Department at University of Canterbury, in particular David Healy for his help in the construction of the mirror box used in the project. Also the other Postgraduate students in the department, who were always around to discuss aspects of research and to just generally bounce ideas off of, in particular; Lance Frater, Will Kamp, Dave Smith and Tony Tsai, Robert Turner.

Contents

List of Figures

List of Tables

Addendum

Section 3.3.1, pages 48-54: It should be noted that the frequency measurments taken from the pendulum testing may contain a significant error, as such the measurements are not reliably measured to 3 significant figures. This error is largely because the measurements were taken from data comprising only slightly more than a single period of oscillation and the start and end points of the single cycle were approximated. This error could be reduced significantly by measuring multiple cycles of the oscillation, therefore spreading the error of approximated start and end points over the multiple cycles. As mentioned earlier, in Section 3.3, the reason that only a single oscillation was examined was due to constraints in the amount of onboard memory on the available DSP starter kit.

Section 3.3.1, page 54: The section highlights differences in phase between parallel sensor elements and attributes this to possible sensor element misalignment. A visual inspection of the sensor and its element alignment was conducted, but due to the construction of the sensor it was difficult to verify if the elements were misaligned. This was largely due to the top sensor platform, which prevented a top down view of the sensor elements.

Also note that the misalignment comment is intended to propose one possible reason for the phase shift in the output and highlight the need to precisely align the elements in future work. Particularly so that the misalignment possibility could be ruled out if a phase shift is again apparent.

Section 4.1, Equations 4.1-4.5, page 66: The values max and min in these formulae are defined as the maximum and minimum of the individual RGB components for a given coloured pixel.

Section 4.2, Algorithm 1, page 71: Code listing does not contain the morphological erosion followed by dilation described in the text. This process, also known as a morphological opening, is conducted before the call to `cvFindContours(binary image)`.

Chapter 1

Introduction

This document details research and development conducted with the goal of establishing a foundation for research in the field of biomimetics at University of Canterbury (UC). In particular the document covers the design of prototype systems for the measurement of insect movement and of forces exerted by insects during common activities, such as walking, while also explaining the motivation for producing said systems.

The presented research starts with an overview of biomimetics and associated work being conducted around the world. This overview helps outline the major motivating factors which led to this research and development being conducted. The biomimetic background is followed by an investigation into methods and devices that can be used for the measurement of force exerted by insects. This section is followed by background research into movement measurement techniques, in particular techniques associated with computer vision (CV) and how they can be applied to movement measurement. Finally, the background section is completed with an overview of the objectives set out for the research.

The information beyond the initial background research and investigations is largely a documentation of the development and testing of three major components. These are; the prototype force measurement system, the prototype movement measurement system and a graphical user interface (GUI) intended to encapsulate the functionality of the two measurment systems.

Chapter 2

Background

This chapter details the background investigations undertaken at the onset of the research presented in this document. In particular it presents the biological basis that inspired the research. This basis consists of biomimetic research on various animals and is detailed in Section 2.1. Of particular note are the techniques and equipment used within the presented biomimetic research, as these will be useful in building a foundation for the pursuit of biomimetic research at the University of Canterbury.

Given the presented biomimetic research conducted world wide and the associated experimental techniques, presented in Section 2.1, the sections that follow perform a background investigation into the methods and materials that could be used to produce improved equipment for biomimetic research. In particular these sections cover investigations into the measurement of force in Section 2.2 and movement in Section 2.3.

2.1 Biomimetics

Recently in the fields of science and engineering there has been an increase in investigations of natural processes and structures, with the goal of inspiring new solutions and approaches. This increasing trend is largely because researchers are realising that the processes of natural selection has forced many of the structures and systems found in nature to reach a highly optimised and efficient state. The area of research described

above has become known as Biomimetics and is one of the major driving concepts behind the research detailed in this document. The term Biomimetics was first coined to describe work by the American inventor Otto Herbert Schmitt during his work in the field of biomedical engineering [1]. Biomimetics is broadly described as, the study of methods and systems found in nature and their application in the design of engineering systems and modern technology.

This section details some of the recent biomimetic research that has been conducted world wide, with a particular interest in insect research and the ways in which this research has been applied to robotics engineering. The following sections contain an overview of biomimetic research into structure and motion, presented in Section 2.1.1, and an investigation into biological control systems, presented in Section 2.1.2. The review of biomimetic research is then concluded with a brief investigation into biomimetics at UC and the resources available within the University.

2.1.1 Structure and Motion

Over the last few decades there has been an incredible amount of work conducted into the structure and motion of both humans and animals, largely conducted with the goal of understanding the complex motions performed by living animals and understanding the highly optimised structures present within these animals.

This research has highlighted many aspects of animal structure and motion that were previously unknown, but has still left researchers with an incomplete understanding of these complex natural mechanisms. Over the course of the conducted research, many models have been created to explain the running and walking motions of animals, such as the; inverted pendulum, spring-loaded inverted pendulum and lateral leg spring models [2]. The study of these models helped develop an understanding of natural motion that had an impact on engineering design of a hexapedal robot (RHex) [3].

Of particular note in the area of biomechanics and energetics is work carried out by Robert Full *et al* at the Poly-PEDAL Laboratories of University of California, Berkeley. A significant portion of this work is carried out on the death-head cockroach Blaberus discoidalis. This research includes the development of a force platform for the measurement

of total force excerted by the insect on a surface [4, 5], which in turn facilitates investigations into the mechanics of rapid running insects [5, 6, 7]. In other work Full *et al* use a treadmill and high speed cameras to track the movement of running death-head cockroaches [8]. In this work the researchers take 3D measurements from the high speed camera footage using a block to calibrate the cameras. Various points were marked with blobs on the insect and their positions were manually measured from digitised S-VHS tape and the 3D positions of these points calculated using a direct linear transform method in computer software.

Some other interesting articles on biomechanics research conducted at the Poly-PEDAL Laboratories include the structural modelling of the legs of the death-head cockroach. This work included; the creation of a full three dimensional (3D) musculo-skeletal computer model of a death-head cockroach leg [9], and also the modelling of passive mechanical properties of these cockroach legs [10].

Overall the extensive research into the biomechanics, energetics and modelling of insects has lead to the biological inspiration for a multitude of robotics designs. These include such robots as: SPRAWL, RHex, and more [3, 11, 12].

It is worth noting that a large proportion of the recent work mentioned above are beginning to explore the neural control associated with these dynamic systems, with this new area of research opening the door to even greater implications in control system design and implementation.

2.1.2 Biological Control Systems

Research conducted into the movement of insects has lead many researchers to the investigation of the control behind this movement. This has in turn lead to increased curiosity into rhythm generation and the sensory feedback that allows insects to achieve dynamic movement in a large range of environments and under a variety of external disturbances. Ultimately, this curiosity has lead numerous researchers to investigate the neural interactions that drive insect activity [13, 14]. For example one work by Schmitz and Büschges *et al* shows a particularly interesting summation of all known sensory influences in a stick insect joint during walking [15].

The work by Schmitz and Büschges is of particular interest as it investigates the effect of additional sensory input from campaniform sensilla on the motoneuron activity in a stick insect leg joint. Campaniform sensilla have been identified as a sensory organ in the exo-skeleton of insects, which seems to record strain from both internal and external forces [16]. This is interesting because study of these sorts of feedback control interations could provide valuable insight into robotics feedback and control systems.

2.1.3 Biomimetics at University of Canterbury

According to information gathered from members of staff within UC there is a huge potential for biomimetic research to be undertaken within the University and the result of this research applied to solve engineering problems, particularly in the robotics field. This potential has been identified for two major reasons; firstly the large amount of research being conducted in the Biology and Zoology Departments on animals that are unique to New Zealand, and secondly because of the equipment and personelle available in the School of Engineering.

While gathering information on the equipment and techniques currently used for conducting biomimetic research within the University, it was found that there is a lack of robust automated systems for the measurement of movement in animals. As a result this is proposed as a system that would be very useful for carrying out biomimetic research in the future. Also the sort of force measurement work used by Full *et al* has not been previously conducted at UC and as such force sensing equipment would need to be acquired or developed. Such force sensing equipment would also be incredibly useful for conducting sensory feedback work revolving around campaniform sensilla, similar to that conducted by Schmitz and Büschges.

It has been proposed that the initial target for the biomimetic research proposed within this document be the weta. This was proposed largely because the behaviour and anatomy of this insect have been researched in the past by staff at UC, in particular by L. Field [17], but also because weta are closely related to crickets and locusts. Many of the weta species in New Zealand seem to have changed little since the Mesozoic era, and as such research of weta and crickets in conjunction could result in interesting conclusions through the difference between the two. Weta have also been proposed because they hold some significance to New Zealand, largely due to the fact that the majority of Weta species are

endemic to New Zealand.

2.2 Force Sensing Methods

Much of the information presented in Section 2.1.1, documenting work at the Poly-PEDAL laboratory at University of California at Berkeley, uses force measurements of moving animals to forumlate and present conclusions on the mechanics involved in animal movement. However, during the investigation of it was noticed that the force measurement devices used in the experiments, gathered a very general measure of the forces excerted by the subject insects. This lead to the desire to produce a more specific force measurement system, which would facilitate a more specific study of the localiseddynamic structures in insects and other animals.

This section details a background investigation into materials and methods used in force measurement applications, with the goal of finding materials suitable for the design and implementation of a more specific force measurement system than those presented in previous research [4, 5]. The application area of the force measurement system will be initially targeted at insect research.

Force sensing transducers are available in a large variety of different types and sizes, but initial searches found that a large percentage of the force transducers commercially available are for force magnitudes well beyond those associated with insect research. This ultimately lead the background research towards gathering information on three different component types that could be used to develop new force transducers more suited to the force magnitudes associated with this research. These three component types were; metal strain gauges, piezo-resistive silicon materials and piezo-electric materials. Of these three component types, the first two; metal strain gauges and piezo-resistive silicon materials are similar in the way they are used to measure a force, while piezo-electric materials are quite different in their operation. An interesting point worth noting, however, is that the operation of all three types of components are based around the fundementals of cantilever mechanics [18, 19, 20].

A small investigation was also conducted into possible fabrication methods for small force transducers. This lead to the discovery of many studies which dealt with the fabrication

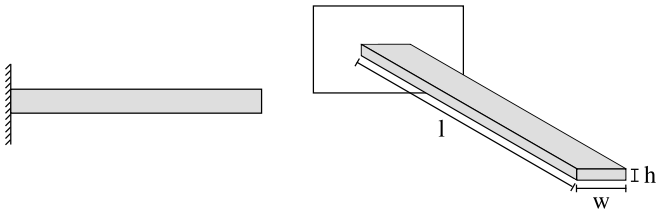

Figure 2.1: A basic centilever beam. Left: A basic side view mechanical diagram. Right: A 3D depiction of the cantilever beam, with dimensions included.

of Micro-electro-mechanical Systems (MEMS) [21, 22, 23]. This work is particularly interesting as the Electrical and Computer Engineering (ECE) department at UC has significant nano and micro-fabrication facilities. These facilities are part of the Nano-structure Engineering, Science and Technology research group.

Presented in Section 2.2.1 is an overview of cantilever mechanics with references to how these machanics apply to measurements force sensing materials and components. Following this introduction to cantilever mechanics are two sections that deal with the common types of component in force measurement applications, these are piezo-resistive and piezo-electric components and are covered in Section 2.2.2 and Section 2.2.3 respectively.

2.2.1 Cantilever Mechanics

A cantilever is a beam structure that is clamped at one end and free on its other end, this is shown in Figure 2.1. Beams fixed in this clamped-free manner have certain quite definite properties, that are often used in various sensor applications. For this reason this section presents the basics of cantilever mechanics.

When a downwards force is applied to a cantilever beam it bends according to its material properties. This end deflection is given by Equation 2.1, where F is the force applied to the end of the beam, l is the beam length, E is Youngs modulus and I is the moment of inertia of the beam [24]. Deflection can also be written with respect to the stress σ, where stress is the force over the area of the cantilever given in Equation 2.2. This is

Stoneys equation [25], and is also shown in Equation 2.1, where ν is Poissons ratio and h is cantilever thickness.

$$\delta = -\frac{Fl^3}{3EI} = \frac{3\sigma(1-\nu)}{E}\left(\frac{l}{h}\right)^2 \tag{2.1}$$

$$\sigma = \frac{F}{A} \tag{2.2}$$

This end deflection causes the top and bottom surfaces of the cantilever beam to be under tension and compression respectively. This is particularly useful because in some cases this opposite tension and compression can be measured, as is the case in piezo-resistive cantilever applications. This is covered further in Section 2.2.2.

The moment of inertia of a rectangular beam, I, with cross sectional dimensions $h \times w$ is given by Equation 2.3.

$$I = \frac{wh^3}{12} \tag{2.3}$$

Using the deflection and inertia of the beam, we can define a spring constant, k, for the cantilever beam, this is given in Equation 2.4.

$$k = \frac{F}{\delta} = \frac{Ewh^3}{3l^3} \tag{2.4}$$

Now given the spring constant, k, of the beam we can use standard resonance equations to calculate the resonant freqency of the beam this is given in Equation 2.5.

$$\omega_0 = \sqrt{\frac{k}{m}} = \sqrt{\frac{Ewh^3}{3l^3m}} \tag{2.5}$$

The major point that should be noted from the resonance frequency shown in Equation 2.5 is that the resonant point is effected by the mass of the cantilever beam. This means that by measuring the frequency of the resonance, the mass of the beam can be determined. Further details on the resonance behaviour of a cantilever beam can be found in [22].

2.2.2 Piezo-resistive Elements

There are two main types of piezo-resistive force sensing devices; metal strain and silicon based devices. The basic principles behind each of these types of device are contained within this section. Also included is a brief description of the electronics used to interface to these devices.

Metal Strain

The first of the resistive strain elements are metal strain gauges. These are based on the simple principles of deformable substances, in particular the deformation of a conductive metal. A common example of strain gauges of this type are simple foil strain gauges, these resistive devices contain a pattern of conductor much like the pattern shown in Figure 2.2.

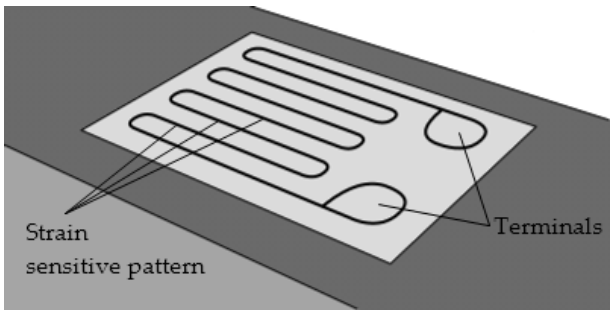

Figure 2.2: An illustration of a foil strain gauge and a typical layout for the conductive strain sensitive pattern.

When subjected to a strain these conductive patterns deform, with this deformation the cross sectional of the conductive materials changes and as a result the resistance of the conductor also changes. Included in Figure 2.3 is an illustration depicting this concept in due to tension and compression.

The specific properties and processes which dictate the operation of a metal strain gauges are those associated with deformation of the metal pattern. Given a long piece of metal with a constant cross section of area A and a length l. If this metal is subjected to a stress, $\sigma = \frac{F}{A}$, where F is the force applied across the cross sectional area. Then the piece of metal will deform, becoming slightly longer with a decreased cross sectional area. This

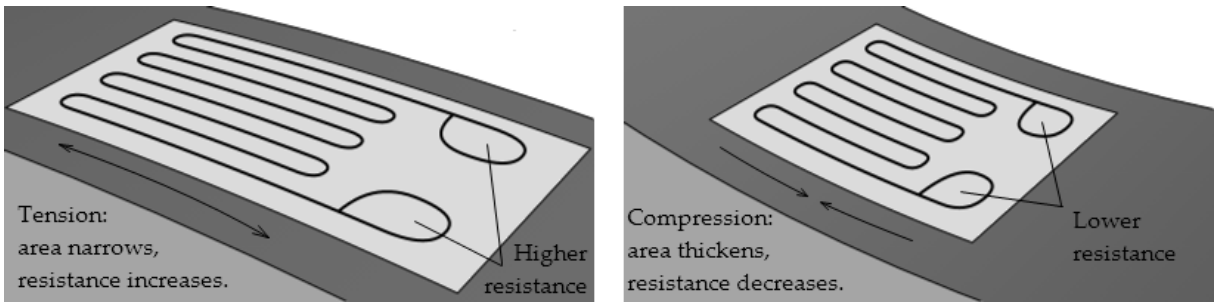

Figure 2.3: An illustration depicting the deformation of a foil strain gauge. Left: The strain gauge depicted under tension. Right: The strain gauge depicted under compression.

results in a relative change in resistance given by Equation 2.6 [21], where R is resistance, ν is the material dependent Poisson's ratio, and ϵ is the relative strain. K is known as the gauge factor and is a to quantify the sensitivity of a strain gauge.

$$\frac{dR}{R} = (1 + 2\nu)\epsilon = K\epsilon \tag{2.6}$$

By using Young's modulus, which is the stress-strain relationship of an elastic material and is defined in Equation 2.7. The change in resistance can then be related to the applied force, as shown in Equation 2.8.

$$E = \frac{\sigma}{\epsilon} = \frac{F}{A}\frac{l}{dl} \tag{2.7}$$

$$\frac{dR}{R} = (1 + 2\nu)\frac{F}{AE} \tag{2.8}$$

The gauge factor above is quite dependant on temperature, this is because the specific conductivity of the metal in the strain gauge fluctuates to a large extent with temperature. For this reason it is nessesary to compensate for temperature when using strain gauges of this sort. This compensation is usually achieved with extra electronics, which usually takes the form of a Wheatstone bridge. Through the use of this form of electronics to interface with the strain gauges the measurements taken from them can be very accurate. This has lead to metal foil strain gauges being used in many commercially available load cells, although as mentioned earlier the majority of these load cells are designed for use with large force magnitudes, far beyond the range associated with insect research.

Silicon

The piezo-resistive effect in silicon is a very different mechanism to that of deformation in metals. While silicon does exhibit some change in resistance due to deformation caused by an applied stress, this is not the major means by which resistance changes. The major means of resistance change in silicon is actually due to the specific conductivity of the silicon, which is itself dependent on stress applied to the silicon. This means that even without deformation, silicon will still exibit a change in resistance due to an applied stress [26].

The relative resistance change that results from an applied force on piezo-resistive silicon has been described in previous works [21]. The relationship between this relative change in resistance R, the material dependent Poisson's ratio ν , transversal and longitudinal relative strains ϵ_t and ϵ_l, and the material piezo-electric coefficients in the transversal and longitudinal directions π_t and π_l, respectively, is given in Equation 2.9. Where E is Young's modulus of the silicon.

$$\frac{dR}{R} = (1 + 2\nu)\epsilon_l + \pi_l E\epsilon_l + \pi_t E\epsilon_t \tag{2.9}$$

Using Young's modulus, shown in Equation 2.7, the resistance change can be related to applied forces as in Equation 2.10. Where F_l and F_t are longitudinal and transversal components of applied force respectively.

$$\frac{dR}{R} = (1 + 2\nu)\frac{F_l}{AE} + \pi_l\frac{F_l}{A} + \pi_t\frac{F_t}{A} \tag{2.10}$$

In a similar way to metal strain gauges, sensor elements construced to make use of the piezo-resistive effect in silicon can also be described by a gauge factor K. Although the gauge factor in silicon is often up to two magnitudes larger than that of metals [26].

These are the type of strain gauges that were used by Full *et al* in the construction of their force platform [4, 5], which was used during some of their investigations into the kinematics of running insects [5, 6, 7].

2.2.3 Piezo-electric Elements

The piezo-electric effect is a characteristic exhibited by some materials, where they develop an electric potential when they have a stress applied. These materials also exhibit the reverse effect, where if a voltage is applied to them their dimensions change, which can result in the element itself excerting a force. This section details some of the basics concepts behind the piezo-electric effect, followed by a short description of ways in which sensors of this type are used.

Piezo-electricity Basics

A piezo-electric material usually has a polarised axis, created during manufacture by applying a large electric field across the material. This polarised axis is the axis in the material along which the voltage potential is developed during the application of an external stress. Given this axis of polarisation it is possible to define some of the modes of operation that a piezo-electric material can posses. These modes are; transverse effect, longitudinal effect and shear effect. During manufacture of a piezo-electric device the material used can be cut in different ways in to make any of these modes the major means by which the device develops charge [27].

Given a piece of piezo-electric material aligned with a standard 3D axis set, with the polarised axis aligned with the z direction. The transverse effect can be described as a generation of charge along the polarised z axis, resulting from a force applied in a direction perpendicular to the polarisation axis. This transverse charge development is dependant on the dimensions of the material and is given in Equation 2.11, where d_{zx} is the piezo-electric coefficient of the material and a and b are the dimensions in the axis of the applied force and the polarisation axis, respectively. The Longitudinal effect is the generation in charge along the polarised axis resulting from a force parallel to the polarised z axis. Longitudinal charge development is strictly proportional to applied force as shown in Equation 2.12. The shear effect results from a shear force applied to the material in the same direction as the polarised axis, this effect is also strictly proportional to force and is given in Equation 2.13. Again in Equation 2.12 and Equation 2.13 the d values correspond to the piezo-electric coefficient of the material in the given mode, this value is explained later in this section. In these equations the n corresponds to the fact that in these two modes multiple layers of material can be stacked, electrically in parallel and mechanically in series, to amplify the effect [27].

$$Q_x = d_{zx} F_x b/a \tag{2.11}$$

$$Q_y = d_{zy} F_y a/b \tag{2.12}$$

$$Q_z = d_{zz} F_z n \tag{2.13}$$

The d values presented in Equation 2.11, Equation 2.12 and Equation 2.13 are the piezo-electric constants relating electric field produced to the applied machanical stress, they are sometimes known as the voltage constants [28]. The subscript on each of these values corresponds to the direction of the developed charge and applied force, for example d_{zx} refers to the charge developed in the z axis direction resulting from a force in the x direction. Sometimes these subscripts are numbered instead with 1, 2 and 3 corresponding to x, y and z. In this numbered notation shear forces sometimes given a seperate definition using a 5. These piezo-electric d constants should not be confused with the very similar g constants, which apply to the inverse piezo-electric effect and relate applied voltage to developed mechanical stress.

Piezo-electric Sensors

Sensors created using piezo-electric materials have been used in many applications including electret microphones. However, the two applications that are more important to this paper are as force and mass sensors. These two applications most often utilise cantilever beams of piezo-electric materials, which are then subjected to either applied force or mass. While the major focus of this research is force sensing, the application of piezo-electric beams as mass sensors is also slightly relevant in that this application uses the active oscillation of the piezo- lectric beam, much like a force measurement method presented by Motoo *et al* [19].

The measurement of force using piezo-electric cantilever beams is usually achieved by simply measuring the voltage developed over the element as discribed earlier in this section. By then taking into consideration the piezo-electric element model shown in Figure 2.4, a measure of the force can be extracted. The measurement of mass on the other hand uses a very different principal. By using the resonance equation for a cantilever beam, shown earlier in Equation 2.5, we can easily see that the mechanical

resonant frequency of the beam is effected by the addition of mass. This means that if the beam is electrically excited at its mechanical resonance in series with a matched impedance, then applying a mass will result in a change resonance, this in turn means more of the excitation voltage will present over the series impedance rather than the element, resulting in a drop in voltage amplitude across the piezo-electric element [19].

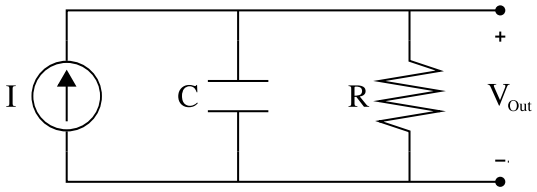

Figure 2.4: Electrical model of a single piezo-electric bimorph element. This is the equivalent circuit attached to measuring devices during DC-coupled operation.

Due to the passive manner in which piezo-electric elements are used to measure force as opposed to the active oscillation required for measuring mass, these modes of operation are often refered to as the DC-coupled or passive and AC-coupled or active modes of operation.

When used in DC-coupled mode equipment is used to directly measure the voltage across the piezo-electric element. Measurements are conducted in this way because the charge developed by the piezo-electric element presents itself across the capacitance of the element. This characteristic is governed by the standard capacitor charge-voltage characteristics, given in Equation 2.14, where V_C is the developed voltage, Q the charge and C the capacitance.

$$V_C = Q/C \tag{2.14}$$

This means that, assuming a high impedance input on the measuring equipment, the dissipation of charge developed during application of force is governed directly by the parallel resistance R, and capacitance C, of the piezo-electric element model in Figure 2.4. The governing property is their resistor-capacitor (RC) time constant τ and is given by the basic relation presented in Equation 2.15.

$$\tau = RC \tag{2.15}$$

According to basic RC circuit physics a developed electric field across the piezo-electric

element of amplitude A will dissipate according to Equation 2.16.

$$V_{out} = Ae^{\frac{-t}{RC}} = Ae^{-t\tau^{-1}} \tag{2.16}$$

Given the characteristics of the exponential and its integral, this means that if we integrate the resulting voltage output for a period of at least 5τ, then this can be assumed to be approximately equal to the integral over all time, as the remaining portion of the integral is negligable with respect to the integral at $t = 5\tau$. Five times the time constant was chosen as this corresponds to a well known exponential decay period, which results in a decay of approximately 97%. Given this approximation the integral is in turn approximately proportional to the initial voltage A, due to the relation shown in Equation 2.17.

$$\int_0^\infty Ae^{-t\tau^{-1}}dt = -A\tau\left[e^{-t\tau^{-1}}\right]_0^\infty = -A\tau \tag{2.17}$$

Given that the initial voltage developed across the piezo-electric element is proportional to Q, the charge developed, and Q is proportional to the applied force F, by a combination of Equation 2.11, Equation 2.12 and Equation 2.13. This means that the integral of the voltage, across a piezo-electric element, over a sufficient time period is an approximate measure of the applied force.

2.3 Movement Measurement

The movement of an insect during various actions can be just as important at the force it exerts on its surroundings. Unfortunately, measuring the movement of an object can be a very difficult exercise, especially when the movement being measured is not along a single defined axis.

Past research, presented in Section 2.1.1, has introduced some different methods used to measure the movement of insects. The major way in which the different methods vary is in whether they attempt isolate the specific movement being studied [15], or attempt to leave the subject unrestricted [8]. For obvious reasons it is often easier to restrict the subject and isolate specific movements, but this is often not desired as the subject my react differently when restrained. Similarly, in some applications devices are attached to the insect being studied [29], however again these can affect the measurements they are taking.

For this reason the majority of background measurement research was conducted in the area of non-restrictive measurement methods. Often these methods involve using high speed video recordings of the insect during experiments [8]. Measurements can then be taken from these recordings and a good measure of actual subject movement calculated using various geometric calculations. Historically, many of these measurements and calculations were carried out by the observer. This is often the case with past research at UC as mentioned in Section 2.1.3. However in recent years CV techniques have opened the opportunity to automate some these systems.

CV research presents a large variety of possible ways in which measurements of position can be conducted without restraining or otherwise hindering a subject. These techniques have the added advantage that they can be automated over video frames and collated into a complete set of movement data and will therefore greatly minimise the effort and time spent by the observer. However, CV is not necessarily simple and first a means of identifying and tracking objects of interest must be found. This section investigates some of the CV techniques that can be used to find useful image points and features. This is followed by an investigation into how measurements can then be taken between these points and collated into data useful for the proposed insect research.

2.3.1 Feature Detection

Over the years a large range of different techniques have been presented for the identification and classification of image features so that they can be better utilised in various CV applications. Some of these methods, such as; edge detection, corner detection, blob detection, Hough transforms and ellipse fitting, were investigated for use in this research, and as such a brief overview of these techniques is included in this section.

Edge Detection

Edges in an image are defined as pixels around which the values of an image change very sharply [30]. These pixels are important in CV applications as many useful features are often found where an edge occurs. For example the boundaries of objects, their shadows and sharp angles within objects, often result edges in images. This means that after

finding the edges in an image, often a lot of information can be extracted from them. But first an efficient edge detector must be used to find the edge pixels.

During the development of CV techniques many different methods have been used to detect edge pixels, but the one that is probably most often used in recent times is Canny's edge detector. This is largely because Canny's edge detector is considered optimal in a precise mathematical sense [30, 31]. Canny's detector was designed mathematically to be optimal in edges which conform to a certain model. This model being a step change, corrupted by Gaussian noise.

The Canny edge detector algorithm has three main steps that it applies to image data. These three steps are also found in many other edge detectors, although they are implemented in variety of different ways and with different overall results. The main steps are as follows:

1. Noise Smoothing
   Through the use of a Gaussian filter mask in Canny.

2. Edge Enhancement
   By applying edge enhancement filter. (Canny's filter is similar in shape to the derivative of a Gaussian).

3. Edge Localisation
   Implemented in Canny using non-maxima suppression and thresholding.

The end result of the edge detection process is a binary image containing the located edge pixels. An example of applying the Canny edge detector to an image of a model weta is presented in Figure 2.5.

If we examine Figure 2.5 we can easily see why thresholding is required. The middle image with a low threshold value allows the majority of detected edges to be displayed. This results in a large number of small edges that result from image noise, these small edges clutter and obscure the image. The right image however, has a better threshold, which results in a very distinct outline of the weta model.

Edge detection can be considered quite a robust operation, although it often requires a large amount of supervision and input from an individual. Unfortunately in most image

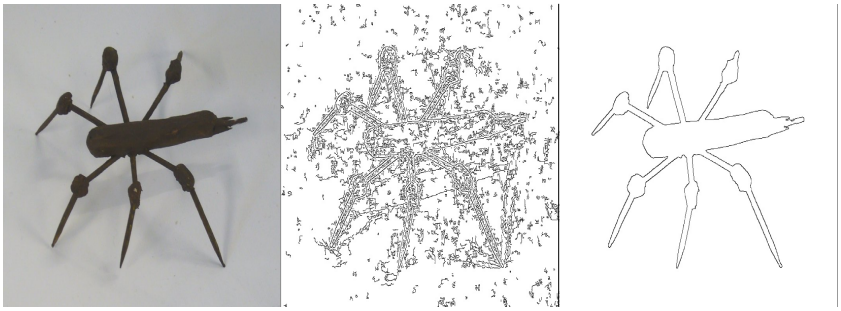

Figure 2.5: The application of the Canny edge detector on a model weta image. Smoothing is achieved by a 7 7 pixel gaussian smoothing kernal. After which the canny algorithm is applied. Left: The original image. Middle: Image after Canny detector applied with a very low threshold of 10. Right: Image after Canny detector applied with a threshold, more suitable for this image, of 160. A model weta was chosen as the subject of this example as the weta has been proposed as the initial target for biomimetic research, as stated in Section 2.1.3.

scenes there are a huge number of edges, many of which are not important to the specific application. This means that it can be very difficult to sort through and determine which edges are important and which edges are not.

Corner Detection

A corner is usually defined as an point there there are two definite edges of different directions, and are important in CV applications because they are often relatively stable across sequences of images or between difference views of a scene. This means that these points can be very useful in object tracking.

Corner points can be found by calculating the partial derivatives of an image neighbourhood, as this image neighbourhood passes over the entire grey scale image. If we use the partial derivatives, E_x and E_y, in a neighbourhood around point p, as shown in Equation 2.18.

$$E_x = \frac{\delta E}{\delta x} \quad E_y = \frac{\delta E}{\delta y} \tag{2.18}$$

We can use these partial derivatives to form a matrix C that characterises the structure

of grey levels around point p, where C is given in Equation 2.19.

$$C = \begin{bmatrix} \Sigma E_x^2 & \Sigma E_x E_y \\ \Sigma E_x E_y & \Sigma E_y^2 \end{bmatrix} \tag{2.19}$$

The reason why this matrix characterises the grey level structure in the pixel neighbourhood is that the eigenvectors of this matrix define the two major linear independent edge directions in the neighbourhood, while their associated eigenvalues encode the strength of the edge [30]. Therefore if the eigenvalues for the neighbourhood are calculated as it passes over the entire image, then by finding points where both eigenvalues are large, we effectively find points with two strong and linearly independent edges. These points, by the earlier definition are corner points. An example of an image of a model weta and some of the corners in the image found through corner detection is presented in Figure 2.6.

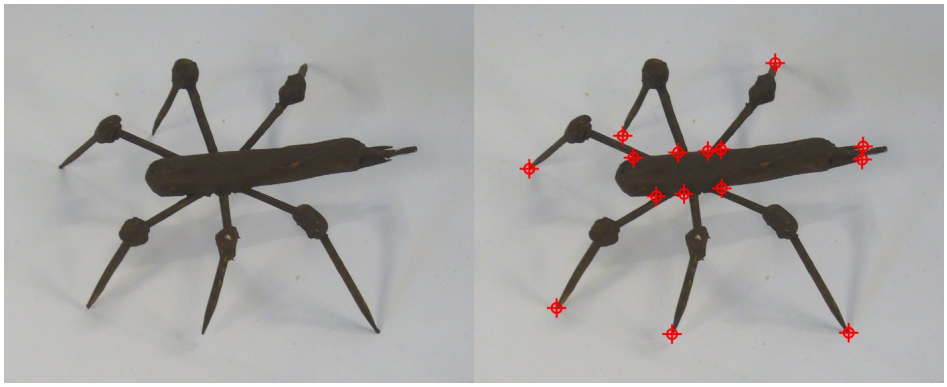

Figure 2.6: The application of a corner detector applied to a model weta image. Left: The origonal image. Right: The image and some detected images. Only some of the detected corners are indicated as to not clutter the image. A model weta was chosen as the subject of this example as the weta has been proposed as the initial target for biomimetic research, as stated in Section 2.1.3.

Hough Transforms

The Hough transform was originally proposed by Paul Hough and is covered by a related 1962 patent. However the transform more often used today is was invented by Richard Duda and Peter Hart in 1972 as an adaption of the original Hough transform [32]. The transforms presented by Hough, Duda and Hart were all used to extract straight lines from

images and are usually performed on the output of another feature detection algorithm, such as an edge detector.

The general concept behind the transforms is that in order to identify a line, all of the pixels that contribute to that line must first be grouped in some way. The original Hough transform achieved this grouping by transforming pixels in the image plane into a parameter space, commonly called Hough space. The Hough transform and Hough space can both be explained more fully by looking at the general formula for a line, shown in Equation 2.20. Where x and y are co-ordinated in the image space, m is the slope of the line and c is the y-axis intercept.

$$y = mx + c \tag{2.20}$$

From Equation 2.20 we can see that the characteristics of a line are not in fact described by the coordinates of any individual point, but instead by the slope and y-axis intercept of the entire line. The original Hough transform used this fact to transform each point in the (x, y) image space into corresponding points in the (m, c) Hough space. Once all points of interest have been transformed into Hough space it is then possible to find one or more maximal points in the Hough space, which correspond to lines that the many points contributed towards.

Since the idea of this transform was first presented it has been improved and adapted in many ways. For example straight line form of the Hough transform, used most often today, created by Richard Duda and Peter Hart proposed that the Hough space could be bounded more precisely by using using a (r, θ) parameter space rather than the original (m, c) parameter space. In this method, lines would be described by the angle θ of the vector from the origin to the closest point on the line, and the distance between this closest point and the origin r. By using these new parameters θ is always bounded to a single revolution and r to the distance in the image farthest from the origin. As opposed to m in the original parameter space which could get very large as lines become more vertical.

Hough transforms have later been expanded even further to cover the parametrisation of even more features. From circles and ellipses to almost any shapes that can be described by a more general set of parameters. The transforms required to transfer into these parameter spaces are all now generally classified as Hough transforms, as they rely on the same basic principals proposed by Hough.

Blob Detection

Blob detection is a method of feature detection that refers to the detection and bounding of connected regions of pixels that share specific properties. Initially blob detection methods were mainly used to find regions of interest, within which further processing would be conducted. Blob detection is also now used to find objects and features, which appear in an image as blob regions. The basics of blob detection are presented here because, with a small amount of initial preperation of an insect subject, blob detection can greatly simplify the movement tracking and measurement process.

Blob detection, in its simplest form as a detector of connected regions, is an algorithm that processes simple black and white binary images with the goal of identifying connected regions of white pixels. Many simple blob detectors require preprocessing to be done on an image to produce this binary image. This preprocessing would ideally mask out pixels that do not meet the specific properties of the desired blobs. However, some application specific blob detectors might form the image mask during the blob extraction process. An example of a simple blob detector might be an algorithm that processes an image and labels all connected pixels, eventually resulting in a label mask which uniquely labels each seperate blob. For this algorithm to be made a definition of connected pixels is required.

Different algorithms use different definitions to define which pixels can be considered as connected. Two of the more common ideas of connected pixels are four and eight connected pixels. In the definition of four connected pixels, a pixel is deemed connected to other pixels of the same value which lie above, below, to the left or to the right of the pixel in question. The idea of eight connected pixels are similar to four connected pixels, except that they are also deemed connected to pixels of the same values in the diagonal directions. These two ideas of connected pixels are presented in Figure 2.7.

The idea of connected pixels is only one way of defining the idea of a blob, and as such there are a number of other more complex blob detectors that use a much more mathematical definition of a blob. Some examples of such methods are the Laplacian of Gaussian, Difference of Gaussians and Determinant of the Hessian approaches [33].

More complex versions of blob detectors will often extract more specific information from the image and present this in a more useful form than a simple label mask. Such algorithms might return the contours that define the individual blobs or multiple small

Figure 2.7: Two definitions of connected pixels showing a single center pixel and the possible surrounding pixels that it could be connected to, given that they are of the same value. Left: Four connected pixels. Right: Eight connected pixels.

image segments containing the each isolated blob, but the the basis of what they achieve is usually the same bounding of regions.

2.3.2 Measurements From Images

Before useful measurements can be obtained from an image, an adequate model of the image capture method must first be constructed. This is important because without such a model it is very difficult to apply structured mathematics to the process of accurately capturing an image. The following is a background investigation into the concepts that allow accurate measurements to be taken from images, these include intrinsic and extrinsic models of cameras, in Section 2.3.2 and Section 2.3.2 respectively, while the basics of stereo vision[1] are presented in Section 2.3.2. Stereo vision was chosen to be the major research target within the CV domain as it is one of the few techniques that allows for full measurement of points in 3D space.

Intrinsic Parameters

One of the simplest models of a camera, and one that works very well when attempting to understand the image capture process, is that of the pinhole camera. This model can be physically thought of first as a large screen with a single very small hole in it, the pinhole screen. This screen is then placed in front of another screen so that light from a 3D scene

[1]The camera modelling descriptions that follow can be found in varying forms in most computer vision publications which deal with stereo vision. This description was formulated after intensive study of two computer vision publications [30, 31], and online of Wikipedia - Pinhole Camera Model.

on the other side of the pinhole screen can pass through the pinhole and strike the back screen forming an inverted two dimensional (2D) image depicting the 3D objects. This concept is illustrated in Figure 2.8.

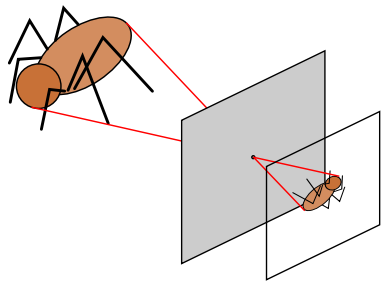

Figure 2.8: A depiction of the physical setup, which defines the basic pinhole camera model.

Through the use of the pinhole camera model we can now define the image capture process in a more mathematical sense. We can define the world reference frame as the 3D scene and the 2D screen as the camera reference frame. During this section it is useful to define points in 3D world reference frame by uppercase letters and their corresponding point in the camera reference frame as lowercase letters with a subscript f. In this way a point $\mathbf{P} = \begin{bmatrix} X & Y & Z \end{bmatrix}^T$ in the world reference frame, has a corresponding point $\mathbf{p_f} = \begin{bmatrix} x_f & y_f & z_f \end{bmatrix}^T$ in the camera reference frame.

Using these definitions we can then model the geometric projection between the two reference frames, this is shown in Figure 2.9. For ease of drawing we place the optical center at the origin of the world reference frame. This is the same as placing the origin in both frames at the same point, displacing the camera frame with respect to the world frame is dealt with later in this section. Also note that due to the effect of light passing through the pinhole, the x and y axis of the camera frame have been mirrored as rays passed through the optical center, so are in the opposite directions to those of the world frame. In classical lense optics this is known as the real image and is the case in Figure 2.9. However, as with most optical systems, a virtual image can also be visualised on the same side as the object, although this image can not be projected onto a screen.

We can also write basic equations of perspective projection between points in the two frames, given in Equation 2.21 and Equation 2.22. It is important to remember that

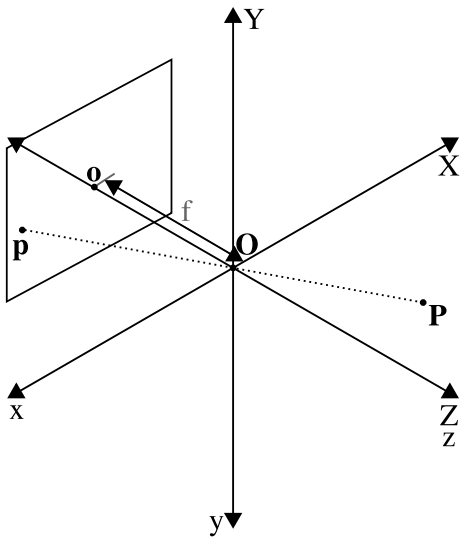

Figure 2.9: Depiction of the pinhole geometric projection between the world reference frame and the camera reference frame.

the camera frame is assumed to be a focal length from the pin hole, or optical center. This means that $z_f = -f$ and therefore points in the camera plane are given as $\mathbf{p_f} = \begin{bmatrix} x_f & y_f & -f \end{bmatrix}^T$. Often the z_f ordinate is assumed, as it is constant, and points written as $\mathbf{p_f} = \begin{bmatrix} x_f & y_f \end{bmatrix}^T$. Note that through the use of these equations the world depth Z is lost and a full reverse transform is therefore not possible. At best a point in the camera frame can be transformed into a line in the world frame.

$$x_f = f\frac{X}{Z} \tag{2.21}$$

$$y_f = f\frac{Y}{Z} \tag{2.22}$$

The next step in the modelling process is usually to transfer points into the normalised camera reference frame. This is the camera frame most refered to in CV applications, largely because through the use of homogeneous coordinate geometry this normalisation is often implied. To normalise the camera frame, points in the plane $z_f = -f$ are refered onto a new plane at $z_f = 1$. This scales the first two ordinates by dividing by $-f$ and tranforms $z_f = 1$. This results in Equation 2.23 and Equation 2.24. For ease of notation points in the normalised camera frame are refered as lowercase letters with a subscript

1, giving points of the form $\mathbf{p_1} = \begin{bmatrix} x_1 & y_1 & 1 \end{bmatrix}^T$ or $\mathbf{p_1} = \begin{bmatrix} x_1 & y_1 \end{bmatrix}^T$.

$$x_1 = -\frac{x_f}{f} \tag{2.23}$$

$$y_1 = -\frac{y_f}{f} \tag{2.24}$$

Unfortunately these equations do no yet relate the world scene to the data stored in an image. In order to do this we must further expand our model so that it can transfer a point into the image reference frame. This is done by incorporating the physical characteristics of the image capture electronics and the principal point of the image. The physical characteristics of the imaging electronics is derived from the size of individual elements in the image capture array, the values are labeled s_x and s_y and are the pixel dimensions in the world reference geometry. While the principal point, with ordinates o_x and o_y, is taken from the translation performed on data in the image reference frame that allows us to index the image from a corner, rather than from the transformed world reference frame origin. The completed transformations are shown in Equation 2.25 and Equation 2.26, with image frame values denoted by lowercase letters with a subscript im.

$$x_{im} = -\frac{x_f}{s_x} + o_x = -f\frac{x_1}{s_x} + o_x \tag{2.25}$$

$$y_{im} = -\frac{y_f}{s_y} + o_y = -f\frac{y_1}{s_y} + o_y \tag{2.26}$$

The information gained about the camera thus far are the internal parameters of the camera and are often colated into a single matrix called the intrinsic matrix. With this information we can now relate points in the normalised camera reference frame $\mathbf{p_1} = \begin{bmatrix} x_1 & y_1 \end{bmatrix}^T$ to actual pixels in the image reference frame $\mathbf{p_{im}} = \begin{bmatrix} u & v \end{bmatrix}^T$, where u and v are quantised to integer values. The intrinsic matrix is denoted by M_{int} and is identified in Equation 2.27.

$$\mathbf{p_{im}} = M_{int}\mathbf{p_1} = \begin{bmatrix} -\frac{f}{s_x} & 0 & o_x \\ 0 & -\frac{f}{s_y} & o_y \\ 0 & 0 & 1 \end{bmatrix} \begin{bmatrix} x_1 \\ y_1 \\ 1 \end{bmatrix} \tag{2.27}$$

Extrinsic Parameters

As mentioned earlier the intrinsic matrix parameters discusses thus far have been derived with the optical center located at the origin of the world reference frame. This is often not the case, especially in stereo vision where there are two cameras that can not occupy the same point and still be of any use. For this reason we now introduce a further two transformations, which are constructed using the extrinsic camera parameters. These transformations come in the form of a 3D translation vector $\mathbf{T}$ and a 3×3 rotation matrix R. The translation vector relates the position of the normalised camera reference frame origin to the position of the world reference frame origin, while the rotation matrix is an orthogonal matrix that relates the axis of the normalised camera reference frame to the axis of the world reference frame via a 3 Degree Of Freedom (DOF) rotation. The transformations between reference frames can be written as Equation 2.28 and Equation 2.29.

$$\mathbf{p_1} = R\mathbf{P} + \mathbf{T} \tag{2.28}$$

$$\mathbf{P} = R^T(\mathbf{p_1} - \mathbf{T}) \tag{2.29}$$

Where R and $\mathbf{T}$ are of the forms shown in Equation 2.30.

$$R = \begin{bmatrix} r_{11} & r_{12} & r_{13} \\ r_{21} & r_{22} & r_{23} \\ r_{31} & r_{32} & r_{33} \end{bmatrix} \qquad \mathbf{T} = \begin{bmatrix} t_x \\ t_y \\ t_z \end{bmatrix} \tag{2.30}$$

The rotation matrix and translation vector can be combined to form the 3×4 extrinsic matrix M_{ext}, such that Equation 2.31 using homogeneous coordinates is true.

$$\mathbf{p_{im}} = \begin{bmatrix} x_{im} \\ y_{im} \\ 1 \end{bmatrix} = M_{int}M_{ext} \begin{bmatrix} X \\ Y \\ Z \\ 1 \end{bmatrix} \tag{2.31}$$

Stereo Vision

Stereo vision is the name given to CV systems that use two or more views of a scene to gain extra information about that scene. In particular it is possible to reconstruct the 3D position of objects visible in at least two scenes. This reconstruction is conducted

using the intrinsice and extrinsic parameters of each of the cameras used to produce the images.

As mentioned earlier in this section, while developing the model for intrinsic camera parameters, during the transformation of points from the 3D world reference frame to the camera reference frame, the depth information of the transfered point is lost. This means that given a point in the camera frame of a single image, the best reconstruction we can hope to make of its 3D position consists of a line projected into the 3D world reference frame. The process of creating this projected line involves transfering both the camera optical center, and the point into the world reference frame. The actual point in 3D space must then lie on the line through the resulting points in the world reference frame. This fact by itself is not very useful, but for each additional image we have that depicts the point of interest we can form another projected line in the 3D world reference frame. By using two or more such projections we can find the intersection of the projected lines and therefore locate the point in 3D space. A diagram depicting this concept for a left and right normalised camera, labeled as L and R, is presented in Figure 2.10.

Unfortunately for a number of reasons, including quantisation error and noise in images, the two projected rays in the 3D world reference frame will almost never intersect perfectly. For this reason we find the two points of closest approach on each projected line. These are the points on each of the lines that are closest to the other line. We then make the assumption that the midpoint of the line segment joining these two points of closest approach is a good estimate of the actual 3D point location.

This reconstruction is relatively easy when the single point of interest has been located in at least two of the available scene images. However using this reconstruction technique soon leads to the consideration of the situation were a number of interest points have been found in each of the images. The problem of correspondence then becomes an issue. This correspondence problem refers the fact that given a point in one image it is not a trivial task to find the same point in the other images, nor is it a trivial task to determine if the point exists in the other images at all.

There are two main method categories used in solving the correspondence problem. The first of these is similarity or correlation based methods, while the second is geometric methods. The correlation based methods work by the theory that the same point in two different images should still have many of the same characteristics. The geometric

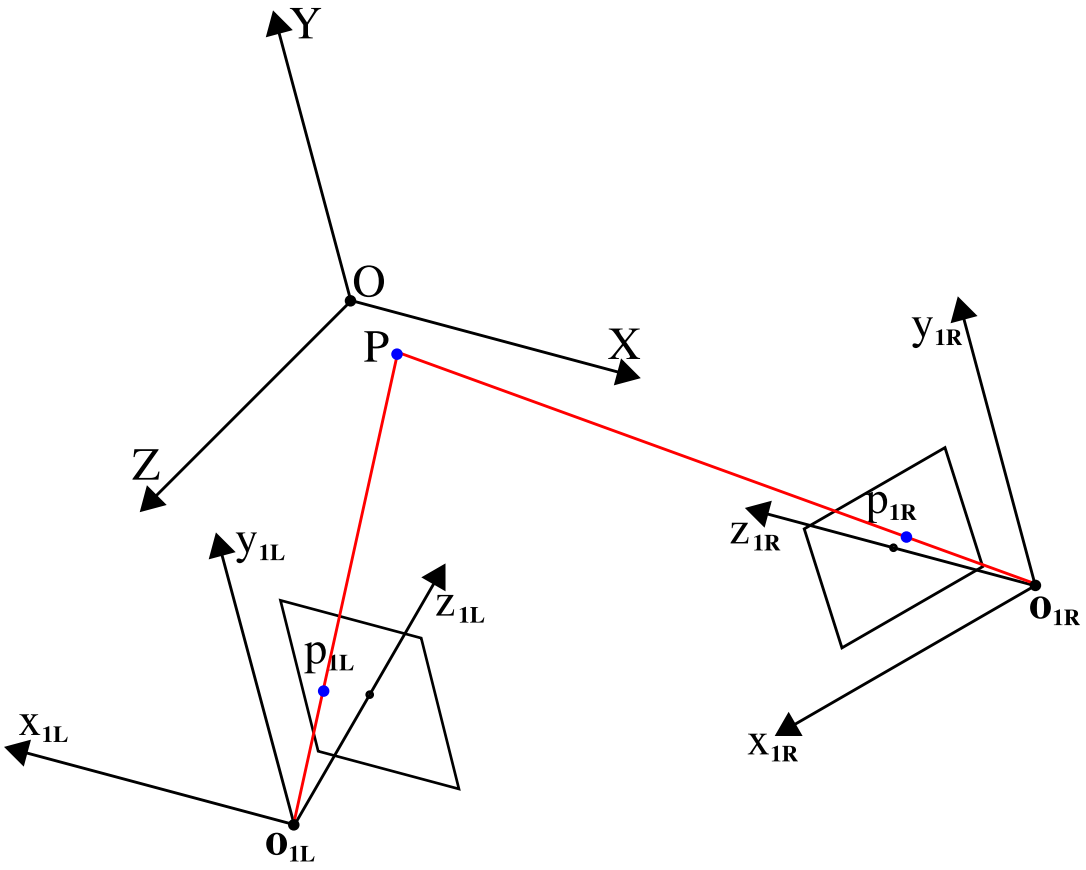

Figure 2.10: A stereo setup containing left and right camera reference frames L and R, viewing the world reference frame. Included is a point $\mathbf{P}$ in the world reference frame and its corresponding points $\mathbf{p_{1L}}$ and $\mathbf{p_{1R}}$ in the left and right camera planes. Rays are projected in the world reference frame through the optical centers $\mathbf{o_{1L}}$ and $\mathbf{o_{1R}}$ of the two normalised camera frames and through each of their projected versions of $\mathbf{P}$. The rays intersect at the point $\mathbf{P}$ in the world reference frame.

methods on the other hand use the geometry of the camera system to reduce the number of possible solutions to the correspondence problem.

One of the more common similarity based methods is that of window correlations. These operate by using a window around each of the interest points to be tested for correspondence. The correlation between the two windows of points to be compared is calculated and the assumption made that if the correlation between the two windows is sufficiently high then the points correspond to one another.

An example of a geometric method on the other hand, is the use of epipolar geometry. Epipolar geometry uses the information contained primarily in the extrinsic parameters of the cameras used to capture the scene views. Consider a two camera system, with left and right cameras labeled L and R respectively. The basis of epipolar geometry are the epipole points, which are the points in each camera reference plane which corresponds to the optical center of the other camera, $\mathbf{e_{1L}}$ and $\mathbf{e_{1R}}$. This point can be found by transfering the optical center of one camera into the world reference frame and then transfering the resulting 3D point into the camera reference frame of the other camera. The result of calculating the epipoles for two cameras with respect to one another is a point in each camera reference plane that lies on the line connecting the optical centers of the two cameras. Now if a point in the left camera $\mathbf{p_{1L}}$ is taken and its corresponding line in the world reference plane found. Then this line and the line between epipoles can be used to define a plane in the world reference plane. This is shown in Figure 2.11.

The key point about this plane is that the line defined by its intersection with the right camera reference plane corresponds to the point $\mathbf{p_{1L}}$ in the left plane. That is to say that the point $\mathbf{p_{1R}}$ in the right camera reference frame corresponding to $\mathbf{p_{1L}}$ must lie along this line. This line is called the epipolar line. The epipolar lines resulting from points $\mathbf{p_{1L}}$ and $\mathbf{p_{1R}}$ can be seen in Figure 2.12.

It is worth noting that while the use of epipolar geometry does not necessarily solve the correspondence problem it does signficantly reduce the number of possible solutions given a large array of points in each image. Another issue is that in real applications there may not be a point that lays directly on the epiline of the other camera, due to quantisation effects and image noise. In this case it it often assumed that the point closest to the epiline, within some limit, is the corresponding point. It should also be remembered that a CV application should probably also deal with the case where a corresponding point does not exist in the other image, either due to the point being occluded in that scene view or that the feature point detection system has not have adequately detected the point.

The basics of epipolar geometry can be presented as a set of transforms known as the essential and fundemental matricies. The essential matrix defines the transformation of a point in one camera reference frame into the camera reference frame of another camera, in world measurement units. While the fundemental matrix defines a similar transform, but this time directly from the image reference frame of one camera to the image frame

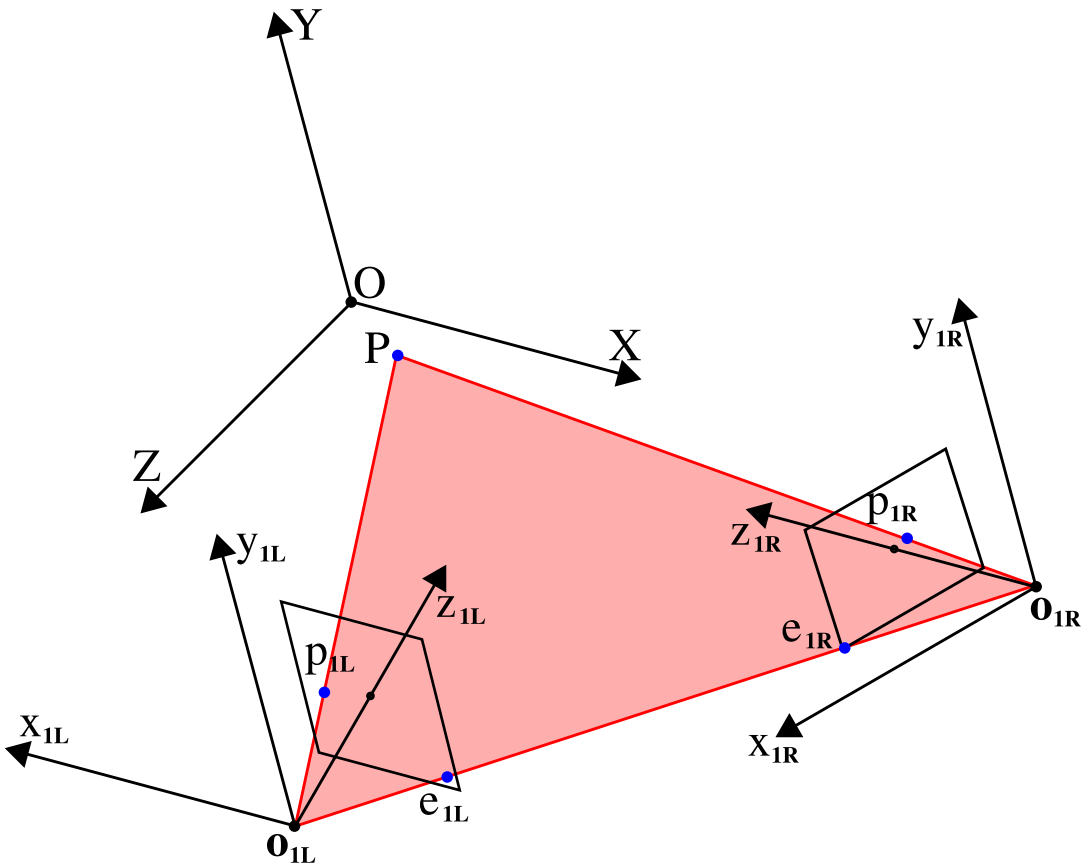

Figure 2.11: A stereo setup containing left and right camera reference frames L and R, viewing the world reference frame. The setup shows the epipolar plane formed by the optical centers of two cameras, $\mathbf{o_{1L}}$ and $\mathbf{o_{1R}}$, and a point $\mathbf{P}$ in the world reference frame. The lines that define the plane pass through the points in the camera reference frames, $\mathbf{p_{1L}}$ and $\mathbf{p_{1R}}$ corresponding to $\mathbf{P}$, and also pass through the epipole points, $\mathbf{e_{1L}}$ and $\mathbf{e_{1R}}$. As a result the plane can be fully defined with knowledge of the two optical centers and either one of the points $\mathbf{p_{1L}}$ or $\mathbf{p_{1R}}$.

of the other camera, in pixel units.

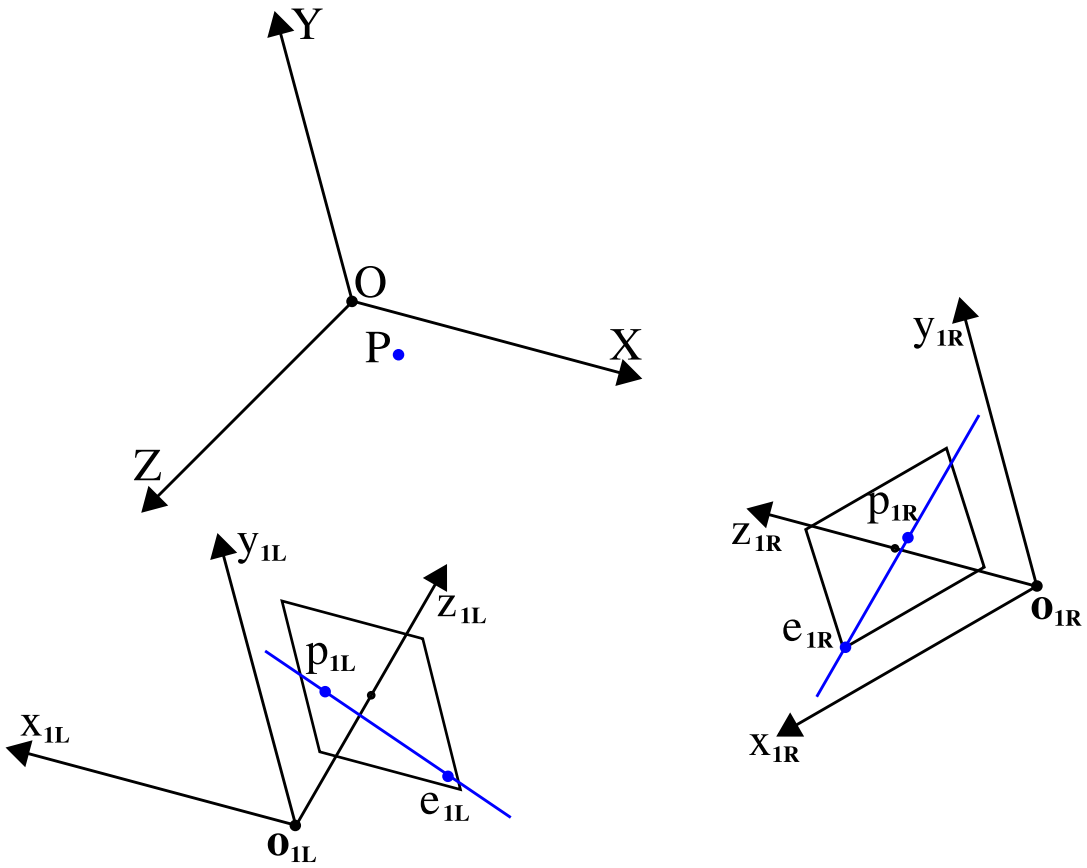

Figure 2.12: A stereo setup containing left and right camera reference frames L and R, viewing the world reference frame. Added to the image are two corresponding points in each of the camera referenc frames, $\mathbf{p_{1L}}$ and $\mathbf{p_{1R}}$, the epipoles in each image frame, $\mathbf{e_{1L}}$ and $\mathbf{e_{1R}}$, and the epilines associated with these points. Given the camera parameters of both cameras and a point in one camera an epiline can be formed in the other camera reference plane, upon which the corresponding point in that camera must lie.

2.4 Overview Of Objectives

After conducting a review of literature on biomimetic research and some of the applications of this research it was decided that the long term goal of the research conducted and recorded in this document will be to provide a foundation to facilitate biomimetic research at UC, in particlar the investigation of movement in insects, the control systems that regulate this movement and the sensory feedback used by the control systems. In

Section 2.1.3, the initial proposed target of this research is identified as the weta, as the behaviour and anatomy of this insect has been previously studied at UC.

It was identified in Section 2.2 that part of the goal of this research would be to produce a force sensor capable of facilitating a more specific investigation of the forces excerted by insects during a range of different behaviours.

It is proposed that in order to produce the force measurements desired an array of miniature force sensors should be produced, in this way the specific forces excerted by an insect at each point of contact with a surface could be investgated. While the full development of such a force sensor array may not be possible within the time scale of this research, it is proposed that an individual force sensor be designed. With the future goal of developing the full sensor array.

This force sensor should have a flat sensor surface, upon which forces would be exerted, given multiple sensors it is proposed that each of the sensor surfaces would be arranged to form a flat surface upon which an insect subject would move and its excerted forces could be measured. The individual sensors should be relatively small, measuring no more than 4mm $\times$ 4mm, allowing for the isolation of a small area, which would be the contact area of an individual insect leg. Sensors should also be able to isolate the measured force into at least its two horizontal DOFs, although seperation of the verticle DOF would also be useful.

As mentioned in Section 2.3 a system for the measurement of insect movement would also be required for biomimetic research at UC. One possible way of producing such a system is through the use of CV techniques, in particular stereo vison. For this reason it is proposed that this research also deal with the research and development of a prototype CV stereo vision system to produce 3D measurements of an insect's movements during experimentation.

Furthermore, it is proposed that in order to increase the overall research value of the developed force and movement systems a computer (GUI) be developed to guide the use of the systems. At this point it is intended that the GUI provide a platform that will link both the movement and force measurement systems, and allow for easier future development of these systems.

Overall is intended that the GUI will eventually reduce the complexity involved in operat-

ing the force and movement systems. So that a researcher, who may not have knowledge of the specifics involved in the measurement systems, could still use the systems to produce useful experimental results.

Chapter 3

Force Sensor

This section deals with the development of the force measurement system as described in Section 2.4. After reviewing the information gathered during the initial background research, it was found that there were no readily available measurement systems suited to the 3D measurements required for insect research. In particular the range of force magnitudes involved are much smaller than those measured by most force sensors. This lack of an appropriate sensor ultimately meant that a new force sensor would need to be developed for the application.

This realisation was followed by a quick review of the resources available at UC and the discovery that the full development of a completed force sensor would not fit within the time frame of the project, particularly if the other goals of the project were also to be undertaken. For this reason it was decided that the force sensor would only be developed to a concept prototype stage, at which point this aspect of the research would be considered completed. This effectively ruled out the use of the micro-fabrication equipment available in the ECE department, mentioned in Section 2.2. This is because the micro-fabrication and testing of a force transducer could easily require a research and development project similar in duration to the research project presented in this document.

The decision to continue up until the prototyping stage of development meant that some of the design requirements could be relaxed to some extent. In particular, this meant that the size requirements could be relaxed slightly to allow for a prototype to be constructed

with available force transducers.

On reviewing commercially available components for force measurement it was found that only small resistive strain gauges, piezo-resistive elements and small piezo-electric vibration elements were of a suitable size range for the desired force sensor. Of these three options the piezo-electric vibration element was the component chosen. This decision was made largely due to successes presented in recent papers, using piezo-electric elements in force measurement applications [23, 19]. With this decision made it is useful to clarify further notation by saying any further references to piezo elements will be in reference to piezo-electric elements, as opposed to piezo-resistive.

The exact piezo-electric element that was purchased for the implementation of the force sensor was selected mainly due to its size and availability. The element was the smallest piezo-electric bimorph element readily available, measuring 15 mm in length, 1.5 mm in width and 0.6 mm in depth across the polarisation axis of the two bimorph plates. A diagram illustrating the polarisation axis with respect to width, length and depth is included in Figure 3.1. It is important to note that in a bimorph element the two plates are polarised in the opposite direction, but along the same axis. Other details on the piezo-electric vibration elements can be found in Appendix A.1.

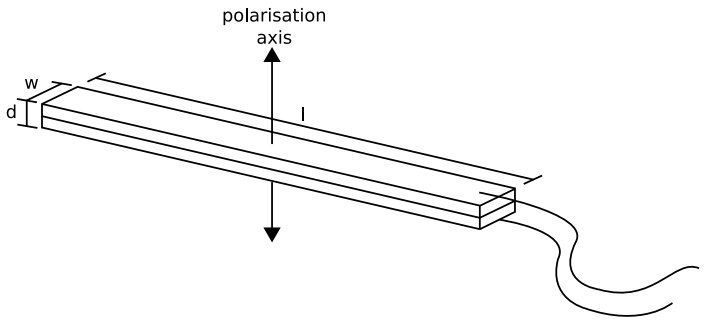

Figure 3.1: Polarisation axis with respect to physical dimensions of piezo-electric bimorph element.

As covered in Section 2.2.3 piezo-electric elements have two main modes, in which they can be used as measurement devices. These are their ac-coupled, or active mode, and their DC-coupled, or passive mode. These two modes are usually defined by whether or not the element is actively oscillated with an external signal. The two modes are more suited to the measurement of different characteristics, with the DC-coupled mode

more suited to force measurements, while the ac-coupled mode provides a very actuare measure of mass. However, there has been some work involving measuring the piezo-electric elements passive charge development during active oscillation of the elements [19]. This method deviates from the normal convention as it does not use the heterodyning techniques usually associated with active oscillation, instead using methods similar to those of DC-coupled operation. For this reason these sorts of methods will be called mixed mode methods in this document.

Of these three modes of operation the DC-coupled and mixed modes are the modes usually associated with force measurement, and as such will be the two modes explored further. However the concepts associated with AC-coupled methods are still discussed as they raise points that could interfere with measurements made by the other methods.

Before the elements can be used in either of the two proposed modes a certain amount of information is required on their operation. For this reason the piezo-electric vibration elements acquired were first characterised in terms of their active and passive characteristics, this is documented in Section 3.1 and Section 3.2. This characterisation was required largely due to a lack of information available from the component retailer, as given the correct information the majority of this information could be determined through calculation.

3.1 Active Characteristics

The mixed mode method presented for measuring force requires a certain amount of knowledge about the piezo elements being used. Most notably the frequency at which the elements should be driven needs to be investigated. It was also realised that because this method relies slightly on the oscillation frequency, the addition of force accompanied by some addition of mass could effect the system in much the same way as frequency is affected in AC-coupled measurement methods. As such this possibility is also investigated to a lesser extent.

The obvious choice for the frequency of operation is the resonant frequency of the piezo-electric element. Unfortunately this was not adequately known from the available information on the piezo-electric vibration elements acquired. For this reason a number of

tests were devised to characterise the frequency response of the piezo elements and also to get a reasonable idea of how this response was effected by the application of mass.

For these tests a single piezo-electric vibration element was connected electrically to a signal generator in series with a 1 MΩ matching resistance. The element was then mechanically mounted onto a printed circuit board with its base 5 mm, measured from the lead end, encased in epoxy resin. The element was then placed in a clamp so that the length of the element projected horizontally into free space. This ensured that the element was securely fastened in the same cantilever manner throughout further single element tests. A figure showing the clamped piezo-electric element and an attached mass during one test is shown in Figure 3.2.

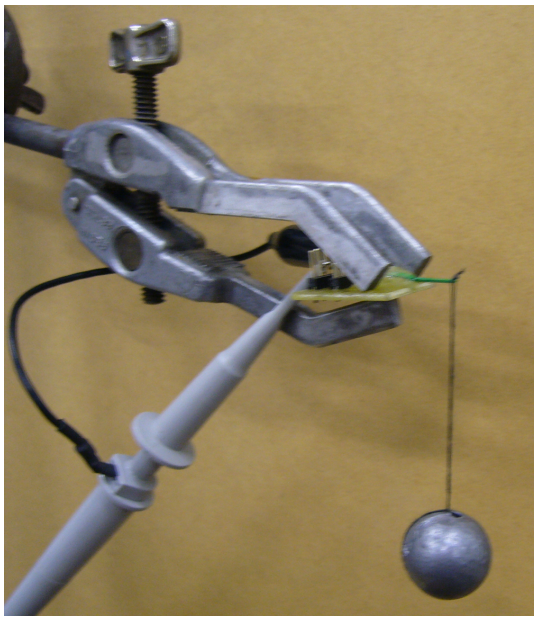

Figure 3.2: Single piezo-electric vibration element, mounted horizontally, supporting mass from end of cantilever arm.

Initially a signal generator was configured to produce a 4 V_{p-p} chirp of 4 s duration, with the chirp frequency varying on a logarithmic scale from 10 Hz to 20 kHz through the duration of each chirp. This signal was then used to excite the piezo-electric element, to gain a rough measurement of the systems electrical frequency response, the results of one such chirp are shown below in Figure 3.3. These results where the result of a screen dump taken from an Agilent 54622D mixed signal oscilloscope.

After the screen dump of the overall chirp had been recorded, the oscilloscope was then

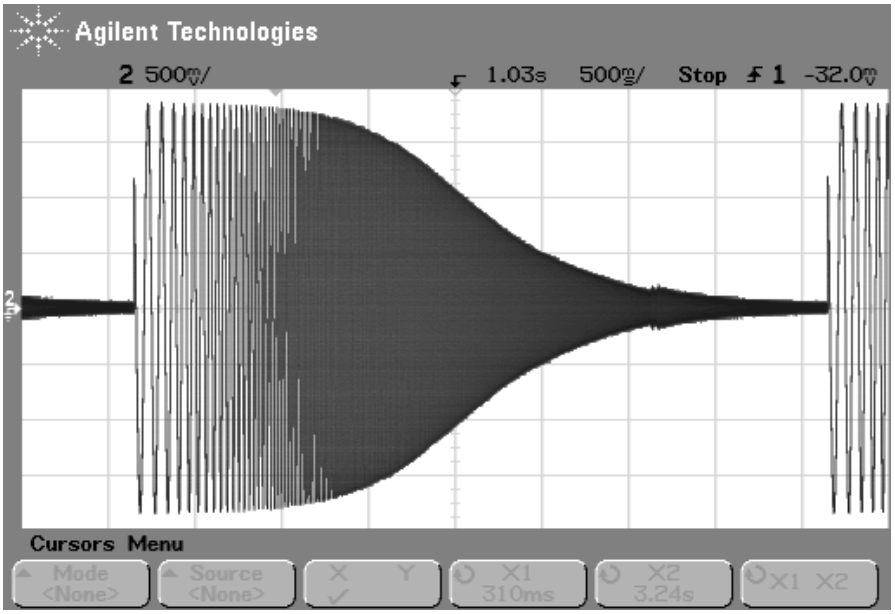

Figure 3.3: Output voltage measurement resulting from 4 V_{p-p} chirp, of 4 s duration and with frequency from 10 Hz to 20 kHz, applied to horizontally mounted piezo-electric vibration element.

used to more accurately measure and record some of the characteristics of the chirp output. Figure 3.4 shows another screen dump from the oscilloscope, this time with added voltage and time resolution.

When the output presented in Figure 3.4 is examined closely, it can be seen that there are three closely grouped peaks in the upper end of the frequency response. The frequencies corresponding to each of the peaks was measured and are presented in Table 3.1, together with the peak amplitude and corresponding attenuation value.

Frequency (kHz)	Amplitude (mV_{p-p})	Gain Level (dB)
2.94	178	-27.0
3.15	184	-26.7
3.33	172	-27.3

Table 3.1: Peak frequencies and amplitudes resulting from chirp applied to horizontally mounted piezo-electric vibration element.

Next in order to investigate the effect of mass on the resonance system, a 7 g mass was attached to the end of the piezo-electric vibration element. The added mass should effect the cantilever system, shifting the resonant frequency. This should be visible when driven

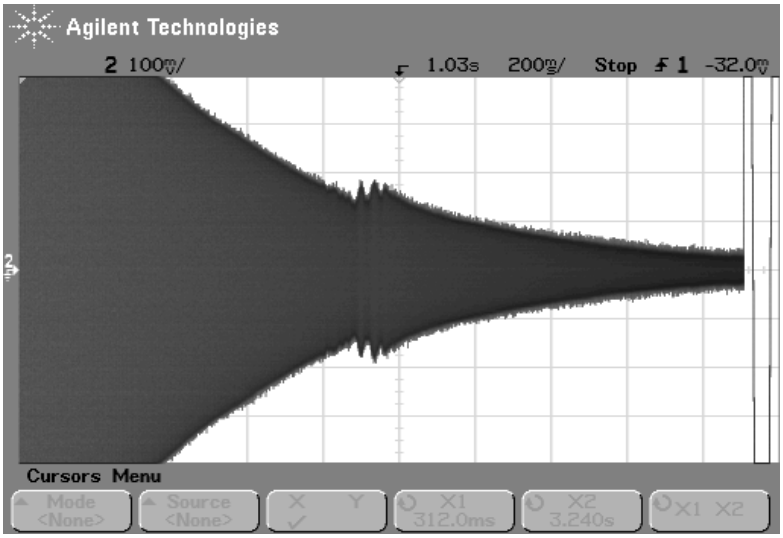

Figure 3.4: Resonance resulting from 4 Vp-p chirp, of 4 s duration and with frequency from 10 Hz to 20 kHz, applied to horizontally mounted piezo-electric vibration element. Voltage resolution has been increased to 100 mV/div, temporal resolution increased to 200 ms/div and the output centered on the resonance points.

by the sinusoidal chirp signal. The chirp result after the application of the additional mass to the cantilever arm can be seen in Figure 3.5. The output was again acquired as a screen dump from an Agilent 54622D mixed signal oscilloscope.

The results from the frequency chirp applied to the piezo-electric vibration element where again analysed more closely, with the specific frequency of some of the more notable characteristic points being measured for closer examination. Another oscilloscope output depicting higher time and voltage resolution is presented in Figure 3.6.

Close examination of Figure 3.6 shows that the addition of mass to the system has significantly changed the characteristics of this upper end of the frequency response. Most notably the three small peaks have been replaced by what looks like two much wider peaks. The amplitude and frequencies of these two peaks were measured and are presented in Table 3.2, along with the attenuation value corresponding to the peak amplitude.

The frequency shifts and outward spread on the resonant peaks are roughly what would be expected with the addition of a mass to the end of the piezo-electric element cantilever arm. Initially this indicates that mass addition may effect force measurements in mixed

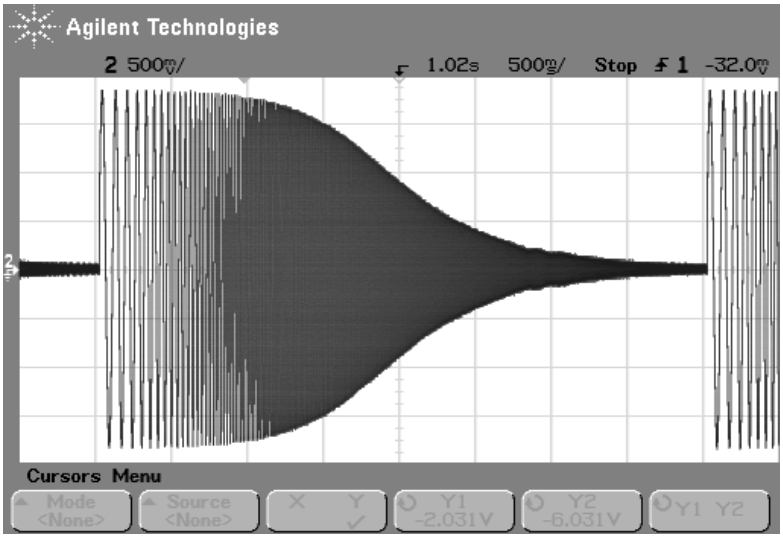

Figure 3.5: Output voltage measurement resulting from 4 Vp-p chirp, of 4 s duration and with frequency from 10 Hz to 20 kHz, applied to horizontally mounted piezo-electric vibration element, while loaded with a 7 g mass at the tip of the cantilever arm.

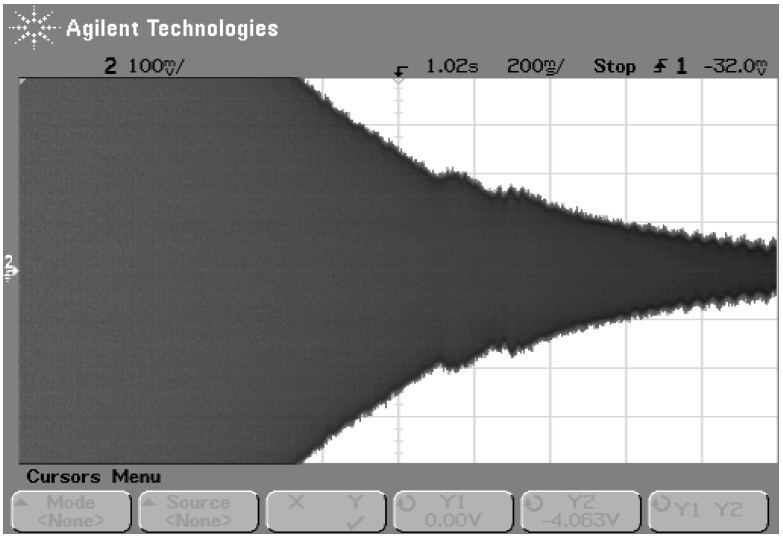

Figure 3.6: Resonance resulting from 4 Vp-p chirp, of 4 s duration and with frequency from 10 Hz to 20 kHz, applied to horizontally mounted piezo-electric vibration element, while loaded with a 7 g mass at the tip of the cantilever arm. Voltage resolution has been increased to 100 mV/div, temporal resolution increased to 200 ms/div and the output centered on the resonance points.

Frequency (kHz)	Amplitude (mV_{p-p})	Gain Level (dB)
2.40	203	-25.9
3.14	169	-27.5

Table 3.2: Peak frequencies and amplitudes resulting from chirp applied to horizontally mounted piezo-electric vibration element, while loaded with a 7 g mass at the end of the cantilever arm.

mode operation, however without more information on the result of mechanically coupling multiple sensors together few further conclusions could be drawn from these initial oscillating element tests. At this point further oscillated tests where postponed until a more complete force sensor, with multiple mechanically coupled piezo-electric elements, was constructed. This information is presented in Section 3.3.

3.2 Passive Characteristics

The passive, or DC-coupled, characteristics of the piezo-electric element are defined by the material properties of the piezo-electric material used, the method of construction and the physical dimensions of the element. In this instance, many of the required electrical results where acquired from the component reseller. These values can be found in Appendix A.1. Of most importance to the passive operation of the elements are the element capacitance, resistance and piezo-electric coefficient, or d coefficient, which relates the electric field produced across the element and mechanical stress applied. The importance of these values has been discussed in Section 2.2.3, along with information on the development and dissipation in piezo-electric materials.

The voltage developed across the piezo-electric elements for a force in the 10 - 1000 N range is slightly smaller than desired. This is the case in most instrumentation applications and easily solved. A simple operational amplifier circuit was produced to increase the amplitude of the signal. The circuit created for this purpose was a simple non-inverting amplifier using a general purpose LMC660 CMOS quad operational amplifier. For which the front page of the datasheet is included in Appendix **??**. Schematics for the non-inverting amplifier design are also included in Appendix B.2. The circuit was designed to impedance match to the piezo-electric element impedance of about 1 MΩ and has a linear voltage gain of approximately 10.

Once the signal was amplified adequately it was then integrated using the oscilloscope so that the measure of force could be verified. An example of the signal resulting from a single loading and unloading with a 7 g mass, associated amplified signal and its integral can all be seen in Figure 3.7. It is expected that each of the loading and unloading interactions be readily apparent on the oscilloscope output, particularly in the integral as this should approximate applied force.

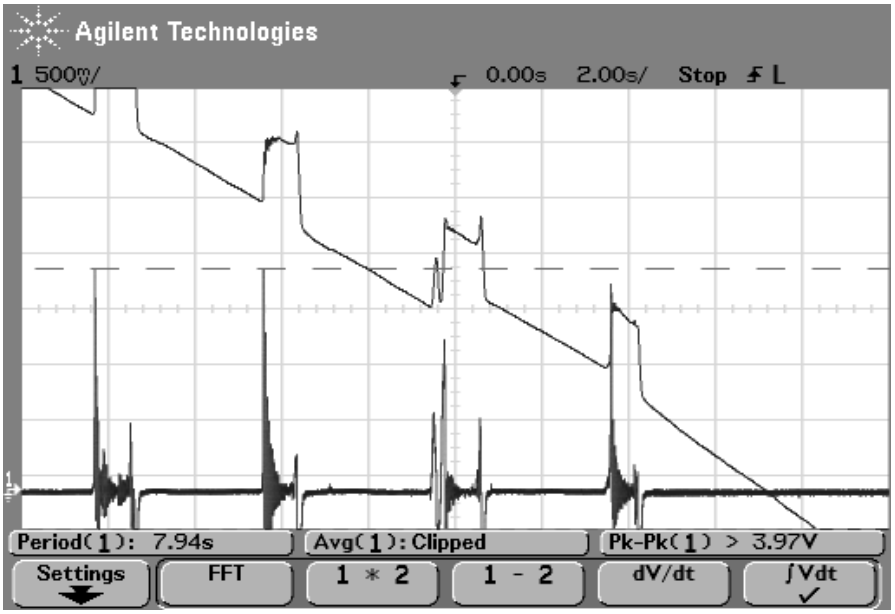

Figure 3.7: Oscilloscope capture of amplified signal across a single horizontally mounted piezo-electric element during multiple loading and unloading with a 7 g mass. Bottom trace shows amplified element signal, while the top trace shows the integral of this signal performed within the oscilloscope.

After examining the presented oscilloscope output, it can be concluded that the signal and associated integral do indeed fit with the expected output. With the signal showing the quick voltage development and dissipation expected from the piezo-electric element model. The integral is quite possibly the most interesting part of this result, as it shows very easily identifiable rise corresponding with element loading and then an equal, in most cases, fall corresponding with element unloading. It is believed that the variation from this behaviour, in the center of this trace, is caused by the addition of external charge due the researcher not being grounded sufficiently, while applying the mass. The almost constant slope overlaying the entire integral trace is attributed to the integration process, this conclusion was reached because the slope varied a considerable amount when viewed at different voltage resolutions, even changing from a negative slope to positive.

It is also worth noting that later tests of this sort will focus on a single loading and unloading so that time resolution can be increased and the specific characteristics can be examined. With this mentioned it is also acceptable to proceed and conduct this further examination as part of later testing.

3.3 Two Degree of Freedom Sensor

The objectives as layed out in Section 2.4 call for the design of a force sensor capable of measuring force in at least two DOF. To achieve this an array of four piezo-electric bimorph elements was proposed. The four elements in the array would be horizontally mounted in a box like shape to maximise their responses to forces in the two horizontal linear DOFs. An overview of the construction steps for this two DOF force sensor is presented in Figure 3.8.

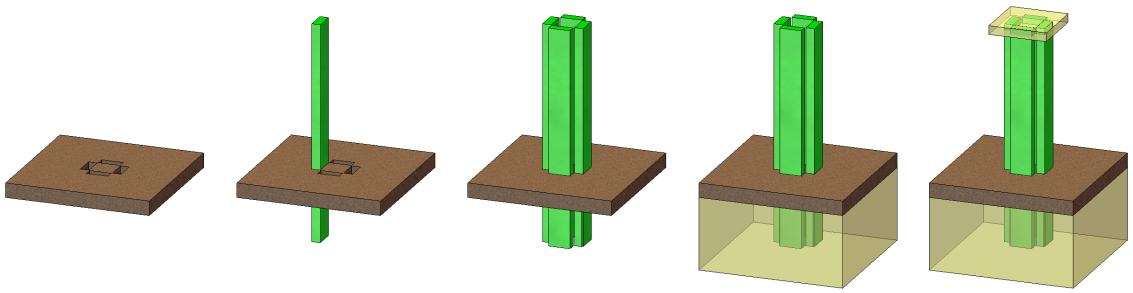

Figure 3.8: Construction stages for the prototype two DOF force sensor.

To assist with the vertical mounting of the four sensor elements it was proposed that a base be made with guide holes to guide the elements and help to keep them straight while their base ends were suitably anchored. This is shown in the first three stages in Figure 3.8. Once these initial steps had been completed it was decided that epoxy resin would make a good final foundation, and also top platform, for the sensor. In order to produce a foundation that would adequately encase the bases of all four elements a mold was constructed. The mold was then filled with epoxy and the base, with attached piezo-electric elements, was placed into the epoxy resin before it cured. The top platform

was made by covering a flat surface in electrical tape and allowing a thin, 1 mm, layer of epoxy resin to cure on top of the tape. The tape was then peeled away and the layer of epoxy cut to size before being attached to the top of the sensor construction.

All of the piezo-electric elements had their electrical connections soldered, tested and had headers added to provide access to the element signals before their bases were encased in the epoxy resin foundation. Each element was connected with their inner piezo-electric plate grounded to a common ground. This ensured that a force perpendicular to a pair of elements would cause a signal of opposite polarity in each.

It is expected that there will be a certain amount of coupling between all four of the piezo-electric elements in the sensor. This coupling will be largely due to the mechanical coupling made by the top sensor platform. Fortunately the coupling should be fairly limited between perpendicular elements, this is because a force through the main axis of one element pair will exert a coupled shear force onto the perpendicular pair. The chosen piezo-electric elements are not designed to develop a large charge from an applied shear forces, so this coupling should result in only small errors. It is believed that any coupling of this form appearing in the sensor outputs will be fairly easily compensated for using a decoupling matrix, the shear effect in the piezo-electric materials is still proportional to force and therefore will be a proportion of one of the other measured signals. Compensation of this sort will not remove all of the coupled error, but will significantly reduce it.

After constructing the prototype force sensor, the obvious next step was to characterise it in terms of its force measuring abilities. Initially it was not immediately obvious which would be the best means of applying a directional force to the top of the force sensor, but this was soon solved by mounting the sensor horizontally, as shown in Figure 3.9. Mounting the sensor in this way with a pin protruding from the center of the sensor platform meant that a mass could be suspended from the base of the pin, which would in turn transfer the force onto the force platform and therefore into the sensor elements. During discussions of the sensor while mounted in this fashion, the elements are given the labels; top, bottom, left and right. These labels have been assigned as if the observer were looking horizontally at the sensor from the direction of the force platform with attached pin.

Once the prototype sensor was mounted correctly and connected to the amplifier, the

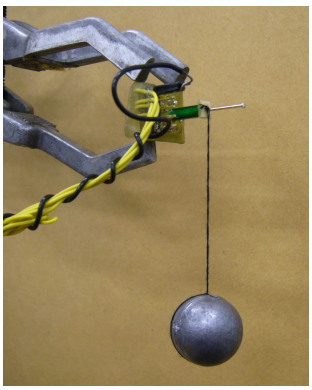

Figure 3.9: Horizontal mounting for prototype force sensor testing.

sensor was put through some simple tests very similar to those conducted on the single piezo-electric element in Section 3.1 and Section 3.2.

The active characteristic tests produced results very different from those of Section 3.1, In particular the resonance peaks apparent in the excitation of the single piezo-electric element were not apparent in the output gained from the full sensor assembly. It was concluded that this was most probably due to the mtchanical coupling between oppositely polarised sensor elements. This is result is promising for the mixed mode opperation of the sensor, but does not help with determining how applied force will effect the oscillation of the system.

At this point tests moved to investigation of the DC-coupled operation of the sensors. This was largely because the DC-coupled mode of operation seemed to be producing more conclusive results. Also the testing of the mixed mode sensor operation required more information on the mechanical properties of the sensor, in particular a mechanical test is needed to determine the mechanical oscillation properties of the sensor. The mixed mode operation of the sensor is an avenue that should be more fully investigated in future works, but is not necessarily required for the development of the force sensor prototype as defined in Section 2.4.

The initial portions of the DC-coupled testing of the prototype sensor were conducted with the element still mounted horizontally as in Figure 3.9. For ease of discussion the same labels; top, bottom, left and right were assigned to the four piezo-electric elements in the sensor, again these were assigned as if an observer were looking horizontally onto the sensor from the direction of the force platform and pin.

The first of the DC-coupled passive tests to be conducted on the sensor structure were again similar to those conducted on the single horizontally mounted piezo-electric element. This consisted of loading and unloading of the sensor structure with a 7 g mass. The output from the top and left sensor elements were captured during one such loading and unloading, these captures are presented in Figure 3.10 and Figure 3.11. In the current mounting setup, the top element sits perpendicular to the direction of force exerted by the added mass. This means that the force is in alignment with the elements polarised axis. As such the signal developed on this element should be larger than the force developed on the left element. This is because the signal on the left element is caused by the force coupling onto this element as a shear force, which should cause significantly less charge development.

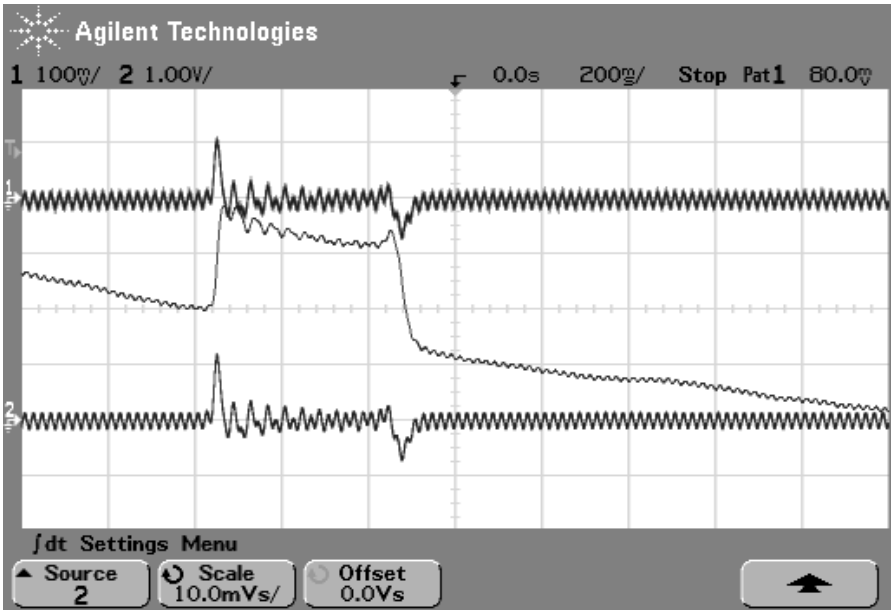

Figure 3.10: Oscilloscope capture of top element signals during single loading and unloading of prototype sensor. Top trace shows unaltered element signal, bottom trace shows amplified signal, while middle trace shows the integral of the amplified signal.

When each of Figure 3.10 and Figure 3.11 are viewed by themselves, they each have the the expected shape associated with a single loading and unloading of a piezo-electric element. Each has very similar characteristics to those of the single element presented in Figure 3.7. When viewed together it can be seen that the left element has significantly less developed charge than the top element. These results are consistent with what would be expected due to shear force coupling. It is important to note that the significant oscillation apparent on the element signal traces is the result of 50 Hz noise coupling

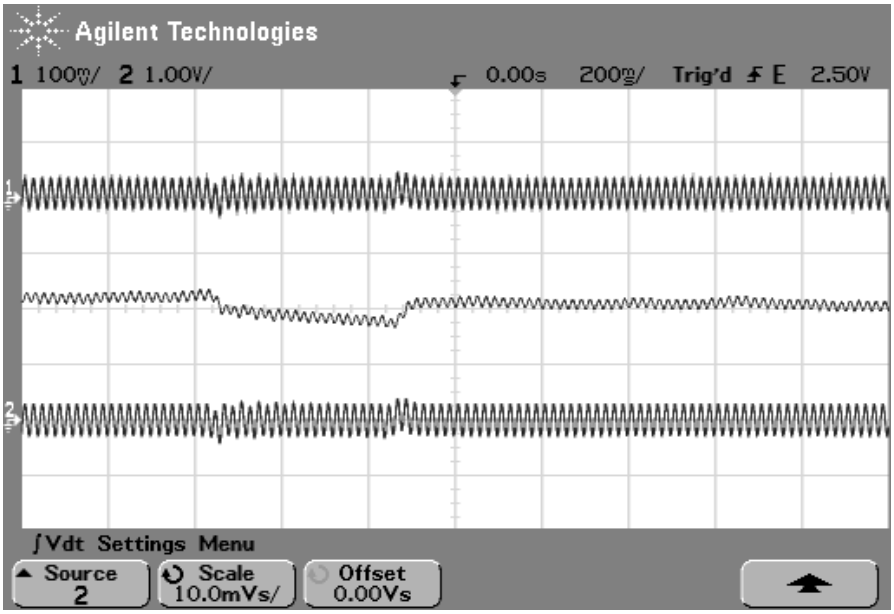

Figure 3.11: Oscilloscope capture of left element signals during single loading and unloading of prototype sensor. Top trace shows unaltered element signal, bottom trace shows amplified signal, while middle trace shows the integral of the amplified signal.

into the system and is dealt with later in this section. Overall the presented signals, their associated amplified measurement and the integral results are all consistent with expectations, showing that the DC-coupled sensor operation initially looks very promising for a force measurement application.

The next requirement was to digitally sample from the amplified sensor signal and analyse these samples. For this task a digital signal processing (DSP) starter kit was used. Specifically a Texas Instruments (TI) C5510 DSP was used. This DSP has significantly more processing power than should be required to sample from a single force sensor and was used mainly because it was the easiest to acquire resource available within the department. The DSP was put to two main uses in this application, first was to sample the signal and second was to remove the integral drift apparent on the oscilloscope trace of Figure 3.7. The signal samples were taken at 8 kHz using the analogue to digital converter (ADC) provided in the onboard audio codec. The drift correction was implemented in software on the DSP, essentially the average signal level was monitored and slowly tracked as samples were processed, this signal average was then deducted from successive samples to remove the DC level and therefore the associated integral drift. Short term DC levels would not be removed by this system due to the very slow rate at which the average was

tracked.

The software on the DSP starter kit was designed to use a ping-pong buffering system, sampling from each of the two available channels of the onboard audio codec. This system allows for the processing of one buffer from each channel, while new samples are being written to the other. Each of the buffers was allocated with space for 4096 samples. This meant that all of the on chip memory of the DSP was allocated for either program or data. Unfortunately this did not allow for a large number of samples to be stored when it came to exporting them for further processing. Also because the audio codec being used for sampling only had two input channels, a maximum of two signals are compared in any of the following experiments.

When the amplified sensor elements were sampled with the DSP board and the sampled data exported for further analysis, it became apparent that there was significant 50 Hz interference coupling into the system electronics from the surroundings. This interference made it almost impossible to interpret anything useful from the sensor signals, so a filter was produced in Matlab to remove the majority of this unwanted frequency component. The filter was implemented using the `fir2()` function available in Matlab. The filter was designed as a 256 tap filter with a notch from 40 Hz to 200 Hz. This filter was found to adequately remove the 50 Hz interference and associated harmonics, while not changing the overall characteristics of the signal traces. Attempts to design filters with a sharper notch cut off was not successful as it proved difficult to produce sharp cut off close to the edges of the 0 to 4000 digital aliasing range. Figure 3.12 shows the effect of the 50 Hz notch filter on one set of samples during testing. It can be easily seen that the notch filter significantly reduced the coupled 50 Hz component making other characteristics in the measurements much easier to see.

3.3.1 Pendulum Testing

The pendulum tests were devised as a means of measuring how the prototype force sensor would react to a varying force in the two measured DOFs. Essentially the forced exerted by a swinging pendulum on its anchor point are very close to sinusoidal, assuming that the angle over which the pendulum swings is small enough in size. This means that a not only can the output from the sensor be tested for varying signals, but also that the system would provide a baseline sinusoidal oscillation frequency to which the outputs could be

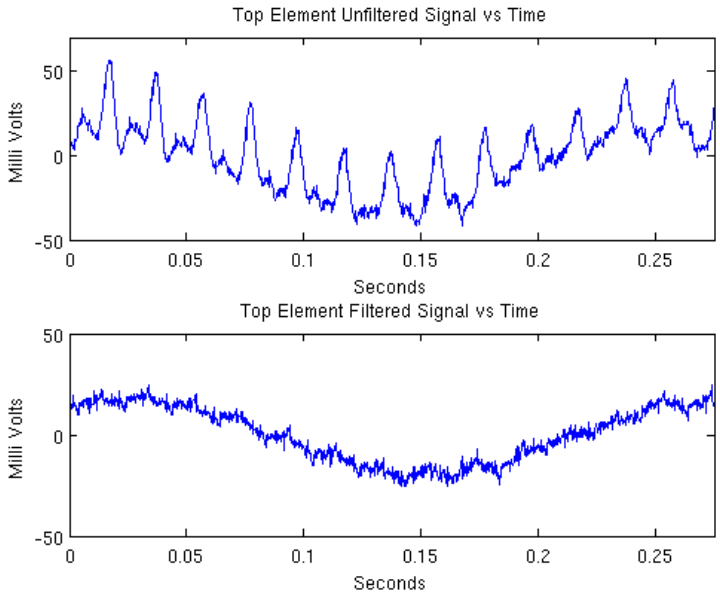

Figure 3.12: An example of a signal sampled from the proposed force sensor, before and after filtering with 50 Hz notch filter.

compared. Also if the outputs are sinusoidal in shape then they can be compared to true sinusoids to give an indication of how linear the sensor force response is over a small range.

For these tests the sensor was again mounted horizontally as depicted previously in Figure 3.9. The elements were labeled as before with the names; top, bottom, left and right, as if they were viewed horizontally from the direction of the sensor force platform and attached pin.

The initial pendulum test was conducted with the DSP sampling from the top and left sensor elements, with the underlying goal of comparing the vertical and horizontal measurements acquired from the swinging pendulum. A sample of the individual element signals after filtering with the 50 Hz notch filter is given in Figure 3.13. The 50 Hz noise is still very noticeable in the signals, but a very noticeable low frequency sinusoidal responce is also apparent. The frequency of this low frequency response was measured to be approximately 3.81 Hz and 3.63 Hz, for the top and left elements respectively, which is very close to the expected pendulum frequency of 4.07 Hz. Little more can be extracted from this data alone, so further processing applied to the signals to aid in further analysis,

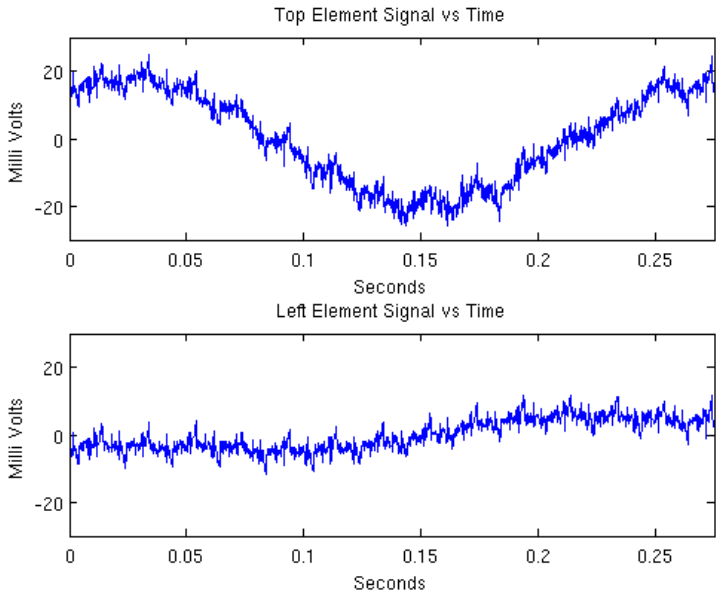

Figure 3.13: The signals attained from top and left piezoelectric elements during pendulum tests.

Each of the signals was integrated to produce an approximation to the force causing the piezo-electric charge to be generated. The result of this integration can be seen in Figure 3.14.

The integration of the sensor signals results in two plots that match the expected force in the two linear DOF. Both are sinusoidal in nature, with the bottom and left element forces approximately 90° out of phase with respect to one another. This result is as expected of the vertical and horizontal forces exerted by a swinging pendulum. When comparing the top element integral to that of the left element it is easily seen that the amplitude of the horizontal force measured by the left element is significantly smaller than the vertical force measured by the top element. This is again consistent with what would be expected from the pendulum setup. As mentioned earlier, there was a shortage in terms of available on chip memory for data samples, for this reason only slightly more than a single oscillation at the pendulum frequency was able to be captured for exporting and further analysis.

The next of the pendulum tests was conducted this time with the DSP connected to the top and bottom element signals. In this way the effect of an equal force on two similarly oriented elements could be measured and compared. The two signals were gain filtered

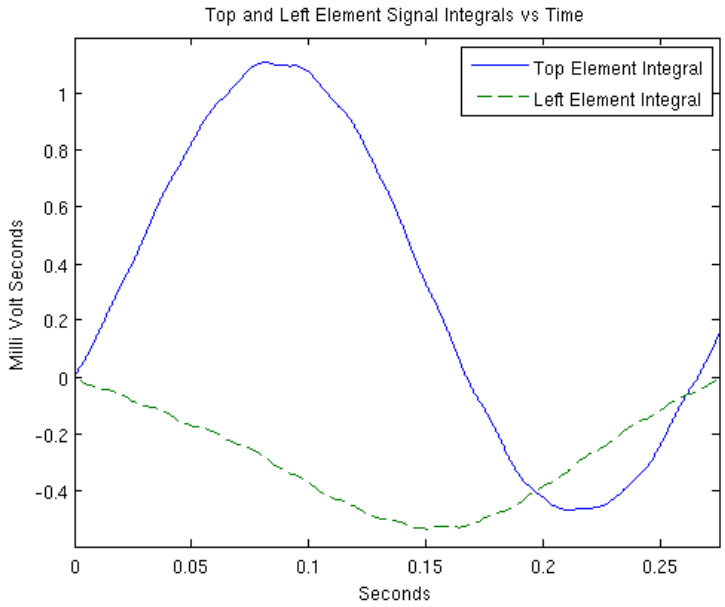

Figure 3.14: The signal integrals attained from top and left piezoelectric elements during pendulum tests.

with a 50 Hz notch filter to remove the majority of the 50 Hz interference present on the measurements. The filtered output from the top and bottom signals can be viewed in Figure 3.15.

Again, as with the top and left measurements, the 50 Hz interference is still visable to some extend over the two traces, however the bottom element seems to have significantly less residual 50 Hz than the top element, suggesting that less noise is coupling into the bottom signal. Again there is a sinusoidal shape to the overall signals with a frequency that is very similar to the expected oscillation rate of the pendulum. The measured frequency in these two traces are 3.84 Hz and 3.78 Hz for the top and bottom traces respectively. The signals were integrated once more in order to compare the result with the force that would be expected on each of the elements. The signal integrals are presented in Figure 3.16

The two resulting integral signals are very similar in form, except that they are essentially 180° out of phase with respect to one another. This is because of the construction of the sensor, which has ground connected to the central surface of each of the four piezo-electric elements. The bottom element trace also seems to have an amplitude which is slightly less than that of the top element. This could be caused by a number of factors, but the

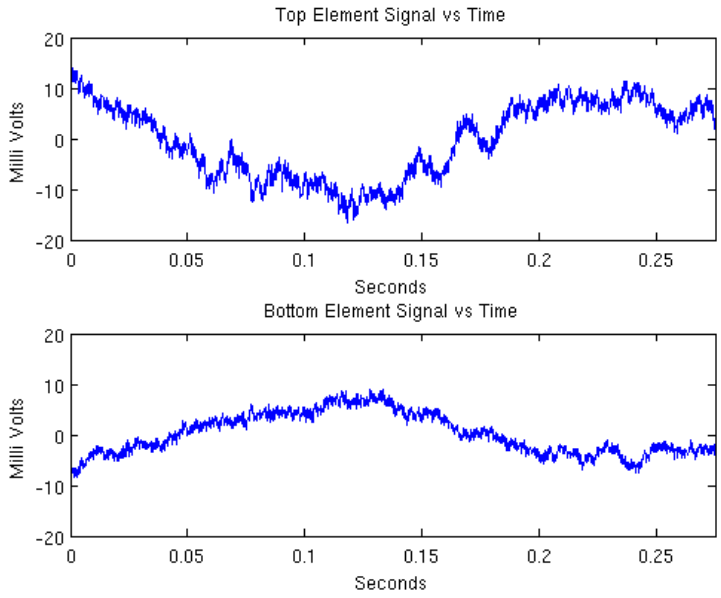

Figure 3.15: The signals attained from top and bottom piezoelectric elements during pendulum tests.

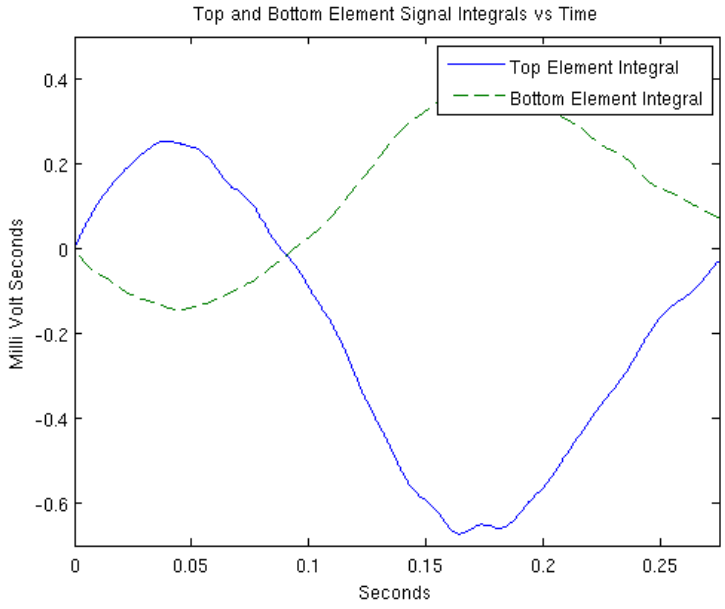

Figure 3.16: The signal integrals attained from top and bottom piezoelectric elements during pendulum tests.

most probable of these factors is a slight miss-alignment of one of the elements, which should be parallel to one another. Another feature worth noting is the disturbance in

the lower portion of the top element integral. From looking at the filtered signal before integration it almost looks as if this is a momentary increase in 50 Hz interference in the system, however there is not enough information to assume that this is the cause of the artifact.

The final pendulum test performed on the horizontally mounted two DOF sensor was to measure from the left and right sensor elements and compare them in much the same way as the top and bottom elements were compared. The filtered measurements resulting from this test are shown in Figure 3.17.

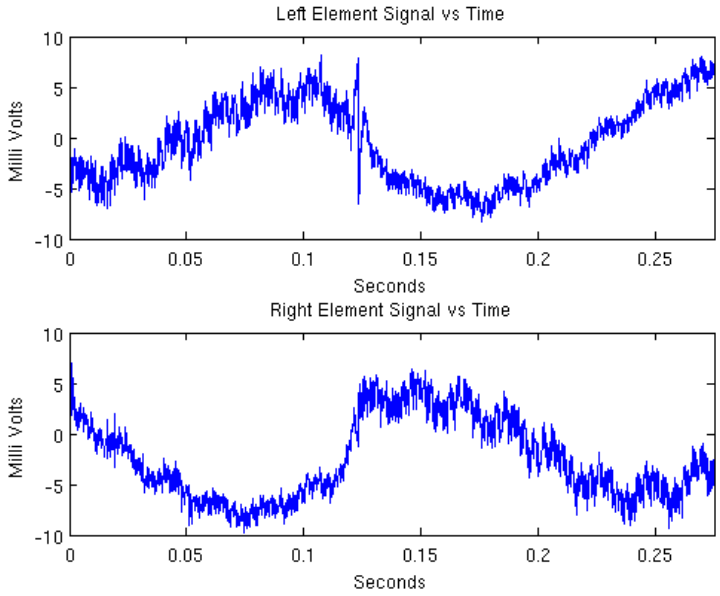

Figure 3.17: The signals attained from left and right piezoelectric elements during pendulum tests.

When examining these two plots they seem to be quite different in their shapes. While they still have a roughly sinusoidal overall shape, the frequency looks slightly higher at first glance. When measured, the lowest frequency component is in fact similar to that expected from the pendulum oscillation. The problem is that the measured signals, in particular the signal gained from the right element, are not quite sinusoidal. To further investigate the characteristics of these two signal plots the integral of each was again taken. The resulting integrals can be found in Figure 3.18.

One of the first things that is noticed when looking at the integral plots is that both the left and right elements have drift between peaks in their oscillation. Another feature that

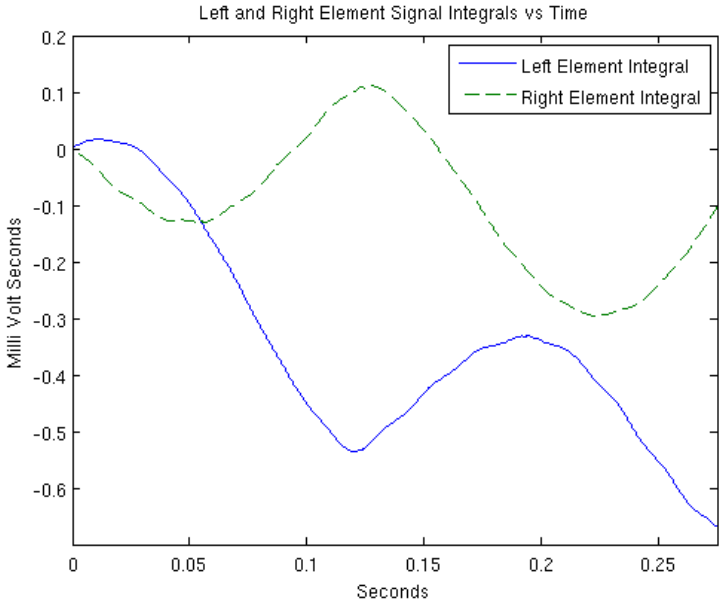

Figure 3.18: The signal integrals attained from left and right piezoelectric elements during pendulum tests.

is readily apparent is the phase shift between the two integrated signals, which should be approximately 180° out of phase with respect to each other. This phase shift can most probably be attributed to error in the construction of the sensor. In particular this significant phase difference indicates that the elements are not parallel to one another. This alignment error was also apparent in the top and bottom elements, although it is much more pronounced between the left and right sensor elements.

3.3.2 Drop Testing

To further explore the possible measurements that could be taken using the constructed sensor, a test was devised to investigate how signals would be effected by a direct downwards force on the force sensor when mounted upright for normal operation. It is proposed that it may be possible to measure the vertical DOF using the common component in all four sensors. To test this theory the prototype force sensor was mounted vertically in a small clamp, as shown in Figure 3.19. Once securely anchored in this position a 42.5 g mass was dropped from a distance of 20 mm onto the top platform of the sensor. The resulting signal on the left and back most element was recorded and analysed to see how

well the force coupled into the two sensor elements.

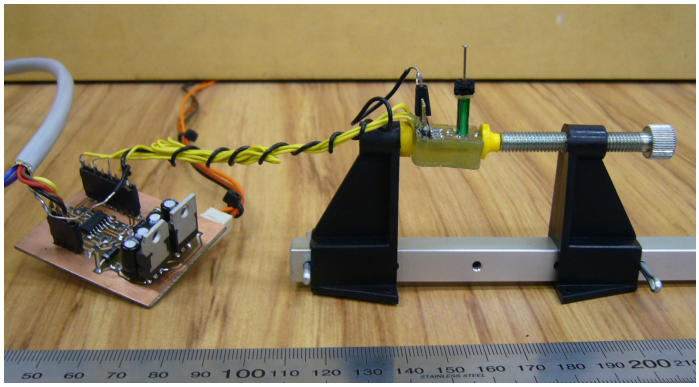

Figure 3.19: Prototype force sensor setup for drop tests.

Initial testing found that the impact of the mass on the hard surface of the sensor platform caused significant minuscule bounces that made the sensor signal difficult to interpret. Also after initial impact the mass would roll off of the top platform adding further unwanted artifacts to the sensor output. For these reasons a small foam pad and vertical pin were added to the sensor platform. The foam intended to slightly damp the impact of the mass and the pin to prevent the mass from leaving the platform. Measured sensor results from one of the drop tests are shown in Figure 3.20, with their integral presented in Figure 3.21.

The two signal responses look very similar to each other which would indicate a good common coupling between the two linear DOFs. Their integrals also look promising in the fact that the force exerted on the sensor has caused a very similar signal integral response in both the back and left elements. Unfortunately the overall shape of this response, is not what would be expected from the addition of a constant downward force. This is not surprising considering the piezo-electric elements are not manufactured to produce accurate results from a force applied directly on their tip.

3.4 Advanced Sensor Configurations

After the initial design and testing of the two DOF force sensor, it was realised that an additional DOF could be added to the force sensor with a relatively simple change to the arrangement of the piezo-electric elements. Initially the elements were placed vertically

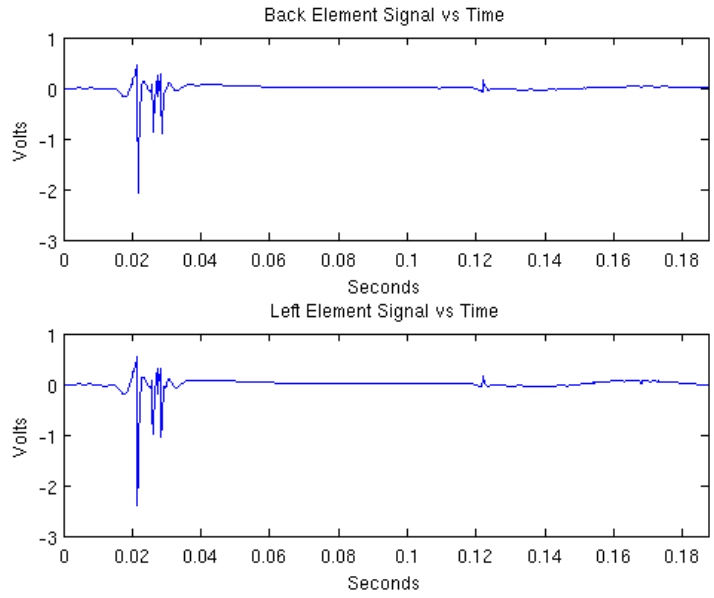

Figure 3.20: The signals attained from back and left piezoelectric elements during drop test.

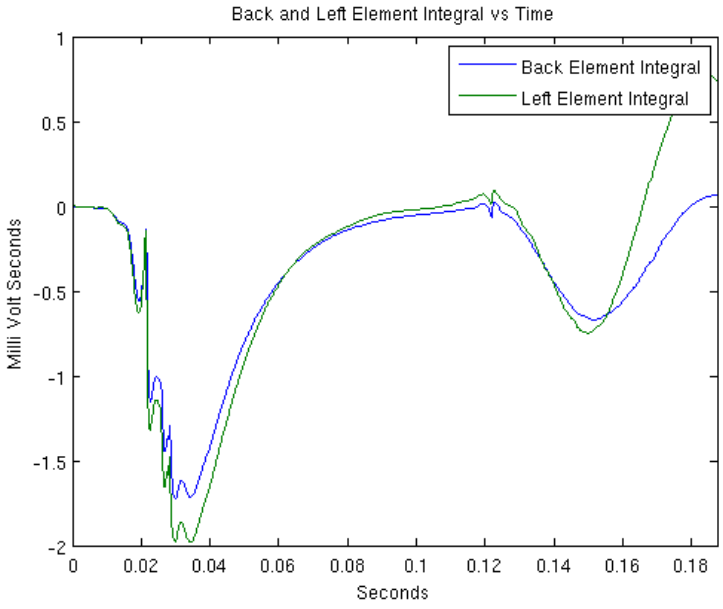

Figure 3.21: The signal integrals attained from back and left piezoelectric elements during drop test.

with their widths forming a square, as it was believed that this would add structural stability. On further consideration, and after a small amount of additional investigation,

it was concluded that torques could be measured in the plane containing the two currently measured linear forces. This would be achieved by positioning the four existing piezoelectric bimorphs in a cross pattern rather than the current square configuration. Figure 3.22 shows the proposed configuration and the stages that would be required to construct such a sensor. The construction of this new sensor configuration would not be any more difficult than the current sensor configuration, although it would use slightly more space. This is because the sensor is now two elements wide in each direction.

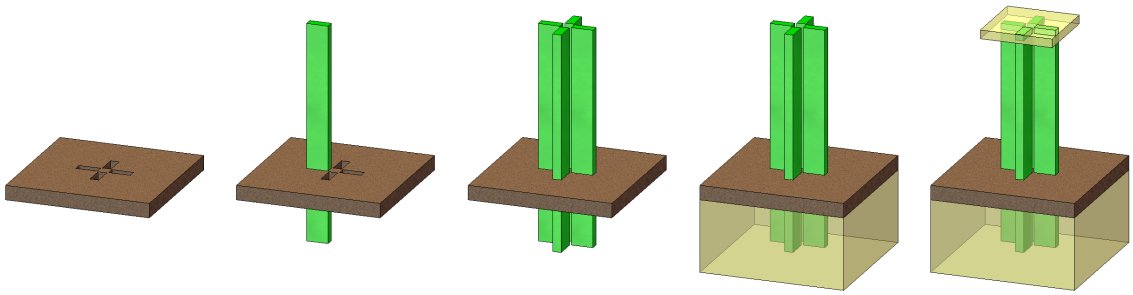

Figure 3.22: Proposed construction stages for an alternative 3 DOF force sensor.

The signal gained from the original two DOF using this new configuration would be very similar to that of the original two DOF sensor. Each of the horizontal measurement axis would have similar signal cross contamination caused by force along one axis acting as a shear force along the elements in the other axis. It is proposed that using this new configuration, torques in the horizontal plane could be determined as they would be apparent as a common component in each of the four sensor elements. Unfortunately this common component would also contain any signal resulting from direct downward force on the sensor. Removal of this downwards contamination could be possible given a measurement of the actual downwards force exerted on the sensor. This downwards measurement could be gained through the attachment of a horizontally mounted piezoelectric element. This in turn leads to the possibility of producing a full six DOF force sensor given four horizontally mounted elements.

The initial stages in producing a six DOF force sensor are very similar to those use to construct the two DOF and proposed three DOF sensors. This is largely because the same vertically mounted elements are required to produce measurements in the two linear horizontal axis and the torque in the horizontal plane. However the process will differ

significantly as additional piezo-electric elements will need to be mounted in the epoxy base of the sensor. This process will be easier if the base can be created in one step, which means that the four horizontal elements will need to be put into position before the epoxy base is added. The first three proposed stages of construction are shown in Figure 3.23.

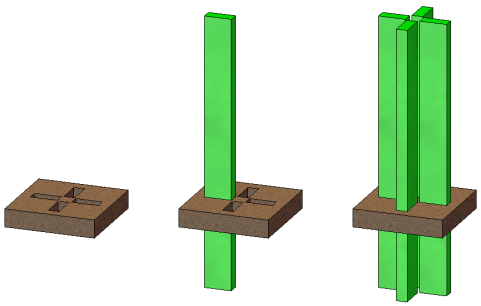

Figure 3.23: Proposed primary construction stages for a 6 DOF force sensor.

Once this initial configuration has been formed, the additional horizontally mounted piezo-electric elements can be added to the sensor. This is shown in Figure 3.24, which depicts the extra stages that would be required in the construction of a full 6 DOF force sensor using the same piezo-electric bimorph elements used throughout this research.

Once the additional four horizontal elements are in place, the bottom of the sensor is encased in epoxy resin much like with the original sensor configurations. This will anchor the bases of the vertical elements, while also coupling the horizontal elements to the point where force is applied at the top of the vertical elements. The next step is to provide an adequate anchorage for the horizontal elements. It is proposed that this will again be provided by encasing the elements in an epoxy resin base. It is important that all four elements be rigidly connected via this base, for structural purposes and so that only forces applied to the center force pad will result in signal. The base should also have sufficient height so that the center "island" is suspended in free space, ensuring that force on the force pad couple into the horizontal elements and not be negated by any other obstruction.

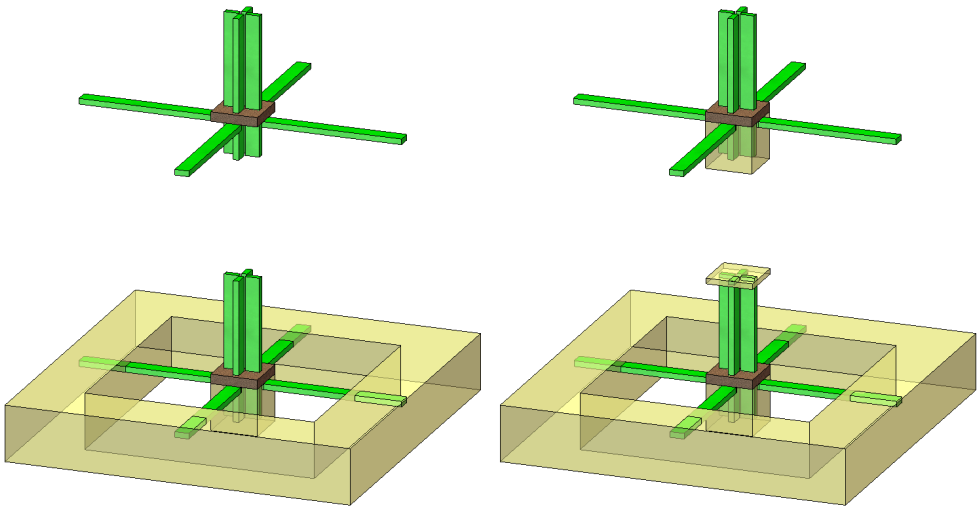

Figure 3.24: Proposed secondary construction stages for a 6 DOF force sensor. Stages proceed from left to right, top to bottom.

3.5 Miniaturisation

The major downfall in the force sensor design was the inability to source sufficiently small piezo-electric elements for the device. The current 2 DOF force sensor prototype measures approximately 20 mm in width, 15 mm depth and 20 mm height, which is much larger than was originally envisaged and means that there is still a lot of work required in reducing sensor size. The majority of this work will most probably be in the development of much smaller piezo-electric bimorph elements, though it may be possible to gain access to elements that are sufficiently small from some other commercial supplier.

Also associated to the size of the sensor is the range of forces it can currently measure. The majority of tests were carried out with one of two different sizes masses exerting their force due to gravity on the sensor. The masses were 7 g and 42.5 g. While the 7 g mass may be considered as being just within the upper range of forces that might be expected in insect research, the 42.5 g mass that was used for pendulum and drop tests definitely is not within the acceptable range. This again as a limitation imposed by the available piezo-electric elements

On of the more promising possibilities is to use MEMS and micro-fabrication techniques to design and implement a new piezo-electric based force sensor. Using these techniques could allow the device to achieve much smaller dimensions and will also give the designer more control over the design of the individual piezo-electric cantilever arms. As noted in Section 2.2, the UC ECE department has facilities that can be used for micro-fabrication. This means that the miniturisation of the force transducer is a definate option for future work.

3.6 Improved Amplification and Noise Reduction

As mentioned in Section 3.3, there was a slight problem encountered during sampling from the prototype force sensor due to noise coupling into the system. This was most apparent in the large 50 Hz component on all of the sampled signals. This interference is obviously not desired and future iterations of the force sensor should include efforts to reduce noise from coupling into the circuit.

Once way of reducing the coupled interference would be to use instrumentation amplifiers for the amplification of the signal, rather than the simple non-inverting amplifier used in this research. In the current design each of the piezo-electric elements has one of their polarised plates connected to ground, this results in a huge amount of noise coupling from the ground into the sensor signals. By disconnecting this grounding of the piezo-electric elements and instead connecting the element directly to the two inputs of an instrumentation amplifier there would be a huge reduction in noise.

The current design uses cables to transmit signals between a few small prototype PCBs. Each of these cables is essentially acting as an antenna for atmospheric interference. One design change that could act to significantly reduce this noise is to place the sensor, amplification and sampling hardware all on a single PCB.

Designing a single PCB also opens a number of other avenues with respect to reducing the overall coupling of environmental noise into the system. These measures include using better ground and power planes, ground plane stitching and use of more decoupling capacitance. Also the physical distance between the differential signals from each piezo-electric element could be reduced to increase common mode rejection.

3.7 Force Plate

The overall intention for the prototype force sensor is to eventually have a large array of the proposed force sensor, arranged so that the top platforms form a flat surface. An insect being studied could then be made to move over the surface and by sampling from the force sensors a complete picture of the forces exerted by the subject could be compiled. This obviously raises some issues, with this research has not yet reached the point where they can be fully investigated.

One of the more important amoung these issues is that of sampling from a large array of sensors. With the current sensor size in the horizontal plane of 5 mm $\times$ 5 mm, covering even a relatively small area of 50 mm $\times$ 50 mm, requires 100 sensors for a total of 400 piezo-electric elements to be sampled from. If we then consider the proposed 6 DOF force sensor, ignoring its larger size at this point, this would further increases the number of piezo-electric elements to 800. With the current sample rate of 8 kHz, this soon becomes a large number of samples. If we then further consider the fact that the data from each element is integrated in software then this also results in a non-trivial amount of processing.

At this point it is worth noting that 8 kHz was well above the sample rate that would be in most cases needed for this application, but this is largely dependent on the RC time constant of the piezo-electric elements in use. So in a future design it is quite probable that one part of the solution to sampling from large arrays will be to simply reduce the sample rate for all elements.

The issues associated with sampling from a large array of sensors can in many instances be compensated for using further electronics. First of all it is proposed that instead of integrating the signal from each piezo-eletric element in software each sensor should be quiped with a small amount of electronics to perform this integration in hardware, specifically a operational amplifier intergrator circuit could be designed to best match the RC time constant of the piezo-electric elements. The output from this integration hardware could then be sampled directly with an appropriate ADC.

Another proposition is to investigate the use of field programmable gate array (FPGA) devices to process and decouple the eight signal samples and transform them into information representing the six DOF of the sensor. It is thought that through the use of

adequate sample hold circuitry multiplexed onto to an array of parallel high speed ADCs a fairly high sampling rate may be able to be achieved over a number of force sensors. The eight data samples from each sensor could then be streamed into FPGA implemented custom decoupling logic.

It is also proposed that methods in the CV domain could be implemented to reduce the number of elements to be sampled from. Due to the nature of the application, in particular the anatomical structure of insects and their size, a large number of the elements in a force sensor array would not be producing any significant signal for the majority of an experiment. It is thought that a CV system could be produced that communicates with the sampling hardware and effectively restricting the elements being sampled from to only those in the direct vicinity of the test subject. Due to the relatively slow speed of CV algorithms, due to large amounts of data being processed, it is thought that method of this restriction and in particular the communication with the sampling hardware will be quite crude, but this idea still shows some promise in solving the sampling problem.

Chapter 4

Movement Measurement

After reviewing the information gathered during the background investigation it was decided that to allow enough time for each of the project's proposed systems to be developed, the movement measurement system should be kept as simple as possible. In order to simplify the complex task of detecting and tracking the pose of the subject insect it was decided that the subject should be marked at critical points. In this way the markings could be detected and tracked allowing for a simpler overall detection system. The other decision that was made during the background research was that stereo vision techniques were the best way in which to calculate truly 3D measurements of an insect test subject.

It was proposed that the marking of the insect should be done by adding spots of coloured paint to the exoskeleton of the subject. This would mean that the markers could be detected in a fairly robust manner using by a relatively simple blob detection algorithm.

Given these design decisions, Section 4.1 presents an investigation into the means of producing a binary image suitable for coloured blob detection, Section 4.2 details the design and implementation of the feature point detection itself, Section 4.3 the stereo vision software, and Section 4.4 contains information on the simple tracking system produced. Finally in Section 4.5 are proposed methods for structure recognition and recording of measurements, presented as possibilities for future work.

The CV algorithms and associated software developed in this section were designed to

make use of the open source computer vision library developed by the Intel Corporation, known as OpenCV. A discussion of OpenCV and why it was chosen as the foundation of the CV software is included in Section 5.1.

4.1 Colour Spaces

The design decision to track coloured markers on the subject insect meant that further investigation into colour detection methods was needed before the research could progress in other areas. For this reason a literature search was conducted into the field of coloured object detection. It was found through this search that there has been a considerable amount of work performed on detecting colours in the red-green-blue (RGB) colour space. This is largely because the majority of image capture devices provide their captured data in the RGB domain. It is worth noting that the RGB colour space is actually a device dependent colour space so it is useful to define a specific RGB domain. Future references to the RGB colour space will be made with reference to the standard RGB colour space as defined by Hewlett-Packard (HP) and Microsoft [34].

The RGB colour space is fairly simple to visualise conceptually as a 3D cube, with each of the three major axis being associated with one of the colors R, G and B. With each axis being bounded from zero to some maximum depending on the colour depth, for example 0-255 for 24 bit "true" colour. A graphical depiction of this is included in Figure 4.1. In this colour space, white is represented by a maximum value for all of R, G and B, while black is the absence of all. Shades of gray lay on the line between black and white, corresponding to by equal R, G and B components.

Much of the work found in the RGB colour space was based around calculating some standard statistical colour properties of the object to be detected, and then selecting pixels which are within some threshold of these statistical values. For example in work by Chung and Shim[35], the mean and standard deviation of RGB colour is calculated across a reference object. The mean in each of the R, G and B spaces is used to define a specific point in the RGB colour space, the distance in the RGB colour space from a pixel value to to this mean is then essentially used as a threshold. The standard deviations are used to define this RGB distance threshold around the specific RGB point. In this way a sphere is defined within the RGB colour space inside of which pixels are of an acceptable

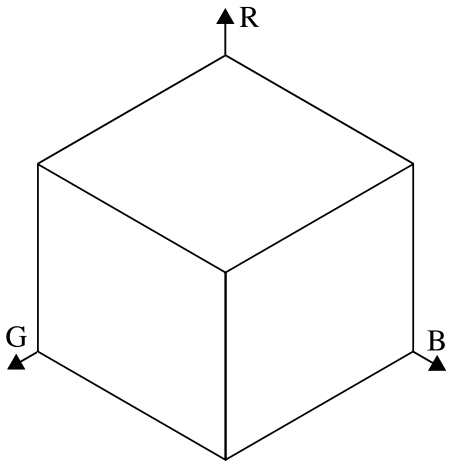

Figure 4.1: The RGB color space can be thought of as a cube. Each of the axis representing one of the colours Red, Green and Blue.

colour to be deemed part of the reference object.

On further examination of this technique it was noticed that this method was not very robust against changes in intensity. In particular changes in illumination have an adverse effect on the correct classification of an object of a given colour. This is a common realisation also identified in other works, for example by Reyes and Dadios [36]. For this reason other methods of isolating specific coloured objects were investigated.

Reyes and Dadios resolve the illumination problem by transforming the RGB color space into a representation independent of illumination intensity. Reyes and Dadios achieved this by using a simple approach of transforming the colour space into chromaticity red, chromaticity green and intensity, which was chosen as it requires very little processing for their embedded real time application. Fortunately any method of colour detection developed for this research would not be affected by real time or embedded processing constraints, and therefore more complex methods could be investigated. To this end the use of the common hue-saturation-value (HSV) and hue-saturation-light (HSL) colour spaces were considered as possible transformations which would reduce dependency on illumination, and as such the following presents a description of HSV and HSL.

The transformations from the RGB colour space to the HSV and HSL are both quite similar. This is largely because the two resultant colour spaces have the same definition

of H, shown in Equation 4.1.

$$H_{HSV} = H_{HSL} = \begin{cases} 0 & \text{if } \max = \min \\ (60^\circ \times \frac{g-b}{\max - \min} + 360^\circ) \mod 360^\circ, & \text{if } \max = r \\ 60^\circ \times \frac{b-r}{\max - \min} + 120^\circ, & \text{if } \max = g \\ 60^\circ \times \frac{r-g}{\max - \min} + 240^\circ, & \text{if } \max = b \end{cases} \tag{4.1}$$

The two colour spaces also have a concept of S, although their equations are quite different and are shown in Equation 4.2 and Equation 4.3 for HSV and HSL respectively.

$$S_{HSV} = \begin{cases} 0, & \text{if } \max = 0 \\ \frac{\max - \min}{\max} = 1 - \frac{\min}{\max}, & \text{otherwise} \end{cases} \tag{4.2}$$

$$S_{HSL} = \begin{cases} 0, & \text{if } \max = \min \\ \frac{\max - \min}{\max + \min} = \frac{\max - \min}{2L_{HSL}}, & \text{if } L_{HSL} \leq \frac{1}{2} \\ \frac{\max - \min}{2 - (\max + \min)} = \frac{\max - \min}{2 - 2L_{HSL}}, & \text{if } L_{HSL} > \frac{1}{2} \end{cases} \tag{4.3}$$

The V and L definitions for the two spaces are also quite similar in concept, although they are again different in their calculation. The transform calculations from RGB shown in Equation 4.4 and Equation 4.5.

$$V_{HSV} = max \tag{4.4}$$

$$L_{HSL} = \frac{1}{2}(max + min) \tag{4.5}$$

In both colour spaces H is essentially the pure colour, and is usually represented as an angle from 0-360∘. S can be thought of as the pureness of the hue, with low values meaning contamination with white light. S is given in the range 0-1. V in HSV can be thought of as the inverse of the amount of black in the colour on the range 0-1, corresponding to black through to no black component. L in HSL is slightly different as it incorporates both black and white on the scale from 0-1, corresponding to black through to white. Using these parameters the HSV and HSL colour spaces essentially isolates illumination from the specific colour.

The HSV colour space is not as easy to visualise conceptually as the RGB colour space. HSV can be thought of as a downwards pointing cone, instead of a cube. The HSV colour space is shown graphically in Figure 4.2. Its parameters are mapped onto the cone as follows; H is the angle around a given circular cross section of the cone, S is the radial

distance out from the center of a given circular cross section, while V is the height at which the circular cross section is taken.

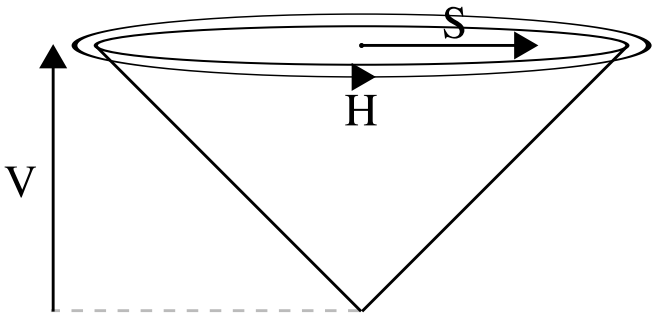

Figure 4.2: The HSV color space can be thought of as a cone. Hue is represented as the angle around the circular cross section, saturation as the radial distance, and value as the height.

In this cone representation of the HSV colour space, black is located at the tip of the cone, white at the center of the top circular face, and pure colours around the top circular edge. This means that all shades of grey are found along the central axis of the colour space cone and of course all other colours are blended in the remaining volume.

The HSL colour space can be visualised in a very similar way to that of the HSV colour space, this is depicted in Figure 4.3. The major difference being that the central axis is drawn out in an upwards direction forming a double cone. If pictured in this way the parameters are mapped onto the double cone in much the same way with; H as the angle around a given circular cross section of the double cone, S is the radial distance out from the center of a given circular cross section, while L is the height at which the circular cross section is taken.

Using double cone representation of the HSL colour space, black is found at the bottom most tip of the double cone and white at the top most. Pure colours are around the circular edge around the middle of the double cone. As a result all shades of grey are again found along the center most axis of the double cone.

Using the RGB, HSV and HSL colour spaces code was produced to perform thresholding on pixels, given a colour space, according to whether their three channel values were with a tolerance range from a specified standard. This thresholding is similar in some ways to

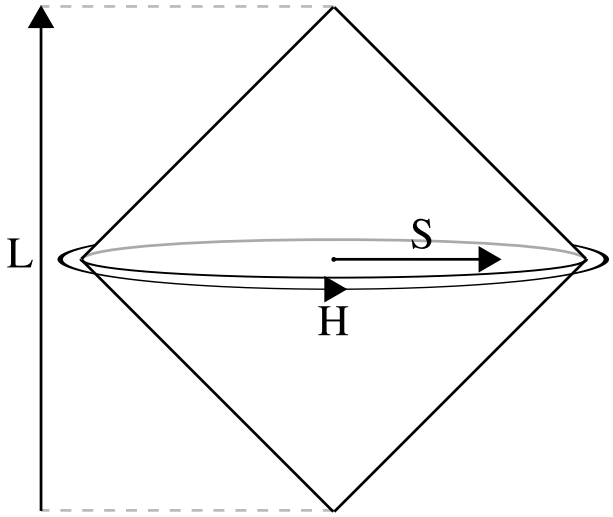

Figure 4.3: The HSL color space can be thought of as a double cone. Hue is represented as the angle around the circular cross section, saturation as the radial distance, and light as the height.

that done by Chung and Shim, except it does not use a distance measure so effectively in RGB space it isolates a cuboid instead of a sphere around the specified value. However using tolerances around a given value in each channel has a very different effect in the HSV and HSL colour domains. A figure depicting the the area in HSV space selected by a tolerances around a given set point is show in in Figure 4.4.

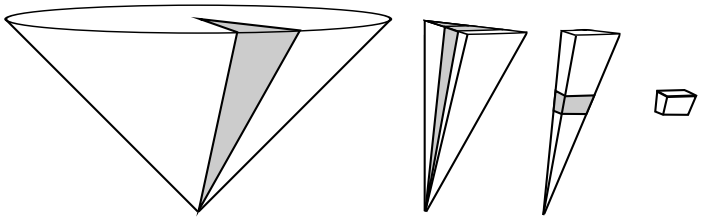

Figure 4.4: The HSV colour space and the effect of three successive tolerance constraints. Progressing left to right; first a tolerance in the H parameter, followed by in S, and finally in V. The result is the selection of a small portion of the colour space.

Applying tolerances to the HSL colour space can be pictured in a very similar way to that of the HSV colour space. The advantage of using the HSV and HSL colour spaces is not readily apparent until one notices that by using a tight tolerance in the H parameter and a very loose tolerance in the remaining two parameters the effect is to bound a sector slice region in the colour space. Values in this slice are of a tight H range but have a large variation in illumination. This is exactly the sort of selectivity that is desired.

4.2 Feature Point Detection

Having investigated a means of isolating pixels of a given colour within an image, the next task was to implement the software that would produce the binary image and process this binary image to extract blob features. Code was implemented so that a colour could be chosen in the any of the three colour spaces explained in Section 4.1. This chosen colour was then stored in a `PixelBound` object along with the chosen tolerances defining desired ranges in each of the three pixel channels. The input image frame was then smoothed with a 3×3 Gaussian blur kernel to reduce effects of noise and the `PixelBound` was applied to the frame pixels to identify those with the desired parameters and create an associated binary image. The resulting binary image then had a single erosion and dilation applied using OpenCV functions `cvErode()` and `cvDilate()`, both with a 3×3 kernel, these processes were applied to further eliminate the result of noise within the image frame. One set of results from applying this tolerance and noise reduction to a single frame is presented in Figure 4.5.

By examining Figure 4.5 we can see the effects of some of the processing applied to the original image. The application of the colour space thresholding results in a binary image that still contains a lot of small errors associated with noise in the original image. However, after the application of the erosion and dilation processes, this noise is completely removed. The end result is a good representation of the desired coloured blobs within the original image.

Given a binary image such as the result in Figure 4.5, the next stage in the blob feature detection is to isolate the individual blobs and extract their specific characteristics. Isolation was achieved using the `cvFindContours` function. This function processes binary images and produces a set of contours which trace the boundaries of the blobs within the

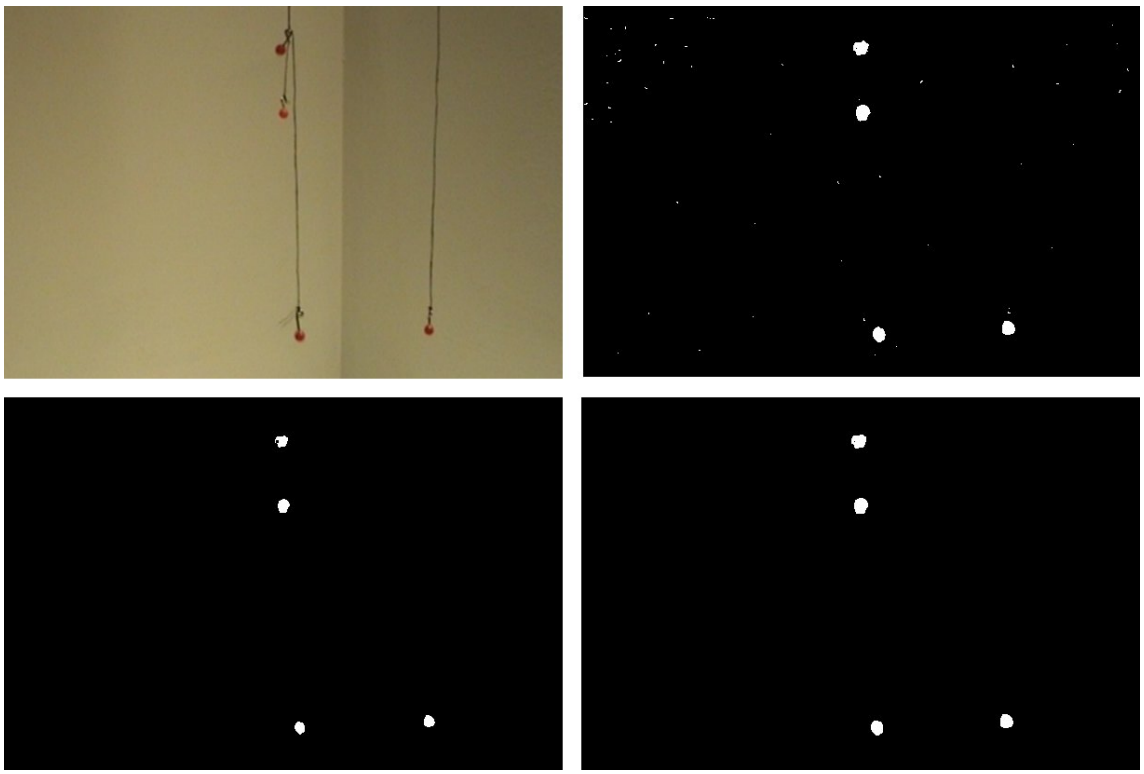

Figure 4.5: Production of a blob binary image by applying; tolerance boundaries, erosion and dilation, to a three channel image in the HSV colour space. Top Left: Original image frame. Top Right: Binary image after application of tolerance boundaries on all three channels, specified point was H = 0, S = 78, V = 69, with tolerances of ±10%, ±40% and ±40% of the total range in H, S and V respectively. Bottom Left: Binary result after erosion with a 3 × 3 kernal. Bottom Right: Final binary image after dilation with a 3 × 3 kernal.

binary image. Information more specific to these blobs can then be extracted from the contour boundaries using a variety of methods. The major information extracted from the blob contours were the spatial moments of the blobs within the bounding contour. The equation for the i and i order moment M_{ij} of an image $I(x, y)$ is given in Equation 4.6.

$$M_{ij} = \sum_{x} \sum_{y} x^i y^j I(x, y) \tag{4.6}$$

The raw moments as calculated using Equation 4.6 can be used to calculate some of the properties of the blob, most notably the blob area, given by M_{00}, and the blob

centroid $(\bar{x}, \bar{y})$, given in Equation 4.7. The calculated information is used to construct new `BlobFeature` objects used in further processing.

$$(\bar{x}, \bar{y}) = \left(\frac{M_{10}}{M_{00}}, \frac{M_{01}}{M_{00}}\right) \tag{4.7}$$

Each of the detected blobs was placed through some final post processing to eliminate impossible and therefore falsely detected blobs. This was implemented by the simplistic means of discarding blobs with insufficient area, width or height, but also by discarding blobs with too large a width and height. The post processing was implemented as a final fail safe to remove blobs that are too small or too large to be the desired markers. It is worth noting that in all conducted tests this post processing was found to be a redundant task, that did not effect the set of detected blob features.

After this final checking the remaining blobs are added to a list and returned by the detection system. The entire process described above for the detection of blob objects is combined and presented as pseudo-code in Algorithm 1.

Algorithm 1 Blob Detection

```
for each Row in Image do
  for each Column in Image do
    if Pixel at (column, row) in Image is within tolerance ranges then
      Pixel at (column, row) in Binary Image = 1
    else
      Pixel at (column, row) in Binary Image = 0
    end if
  end for
end for
call cvFindContours(binary image)
for each Contour found do
  Calculate Contour moments
  if Contour size and moments in acceptable range then
    new Blob(size and moments)
    Add Blob to Blob List
  end if
end for
return Blob List
```

4.3 Stereo Vision

Given the system developed in Section 4.2 for detecting the blob markers placed on a subject insect, the next task in measuring the position and then movement of the insect is to measure the position and movement of the blob markers. As mentioned in the background research presented in Section 2.3.2 one of the few ways of extracting full 3D measurements with CV methods is the technique of stereo vision, for this reason a stereo vision setup was produced.

Initially a separate application was produced to investigate camera calibration. This application was designed to use pictures of a calibration pattern from a stationary camera. By providing the software with multiple images, each containing the calibration pattern in a different alignment. One such image is included in Figure 4.6. The software was able to calibrate a single camera, by first finding the checker board corner image positions using `cvFindChessboardCorners()` and then using these positions, along with the actual checker board dimensions, in the camera calibration function `cvCalibrateCamera2()` to produce an estimate of intrinsic and extrinsic camera parameters. It is interesting to note that this calibration technique is similar to that use by Full *et al* to measure cockroach movement [8].

The camera calibration software was then extended to use two views of the calibration scenes, each from a separate stationary camera, and in this way calibrate two cameras. Functions were then added so that the same point could be selected in each image, and the application would use the intrinsic and extrinsic parameters calculated for each camera to reconstruct the 3D position of the point in space. These functions were then used to test the calibration of the two camera system, by selecting points and measuring the lengths of objects in the image scene. These objects were then physically measured and the results compared. The result of measuring several objects with the CV application and physically can be seen in Table 4.1, also presented in Figure 4.7 is an image from each camera with the selected points marked in the image.

Unfortunately, when it came to further expanding the stereo vision setup, by extending the process to operate on successive frames in video images, it was found that the project only had long term access to a single video capture device. For this reason another method was investigated to produce extra scene views. This method was to place a mirror in such a way that it produced another view of the scene. The extracted view

Figure 6: An example of an image containing a calibration checker board, used for camera calibration.

image would need to be flipped in order to correct for the mirroring process, however other than this flipping, the image should essentially be the same as a view from another angle. The use of a mirror would have the advantage that it would reduce the overall cost of the setup during investigation, with the disadvantage that the effective image area of the camera would be divided between two views, significantly reducing spacial accuracy in each of the view images and therefore overall accuracy in the 3D reconstruction.

During the consideration of alternative means of providing a second video scene view to the system, the possibilities of adding even more views was also discussed. Through the

Object Measured	Calculated Length	Actual Length	Error
Map Pins	151 mm	152 mm $\pm$ 0.5 mm	0.65% $\pm$ 0.33%
DVD Diameter	119 mm	120 mm $\pm$ 0.5 mm	0.83% $\pm$ 0.42%
Drawer Height	115 mm	117 mm $\pm$ 0.5 mm	1.71% $\pm$ 0.43%
Length of A4 Sheet	295 mm	297 mm $\pm$ 0.5 mm	0.67% $\pm$ 0.17%
Cable Ties	59 mm	60 mm $\pm$ 0.5 mm	1.6% $\pm$ 0.8%

Table 1: Comparison of measurements taken using stereo vision application and actual physical measurements.

Figure 4.7: Two images corresponding to a stereo pair. The 3D positions of each of the marked points and the lengths of objects in the scene were calculated using the camera parameters, results are listed in Table 4.1.

use of a third scene view the problem of object occlusion, briefly mentioned at the end of Section 2.3.2, can be greatly reduced. This is of course assuming that there is a large base line between the position of each of the cameras, essentially ensuring that each camera views the scene from a very different angle. This third view could also be achieved with the mirror setup, but would further reduce the spacial resolution available for each view. A frame was built to test the use of one or two mirrors. An image showing this setup is included in Figure 4.8

The concepts used in the design of the initial stereo vision test application were then transferred into the main application, which at this point contained only the blob detection software. During the implementation of the stereo concepts in this application there were a number of problems encountered. It seemed that using a camera facing directly forwards on to the mirror box frame, so as to capture a front view and a side view in the left mirror, caused the calibration software to return an incorrect result. This incorrect result seemed to be a local minima in the solution space that corresponded to a setup with a much smaller base line, with respect to the viewed scene. In the mirror setup the large base line was caused by the mirror producing a view image that was from a position rotated 90° with respect to the original image. For this reason the camera and mirror setup were altered slightly to reduce the base line between the two camera positions. This corresponds to increasing the angle of incidence of light from the image reflecting in the mirror towards the camera, and was achieved by adjusting the camera and mirror

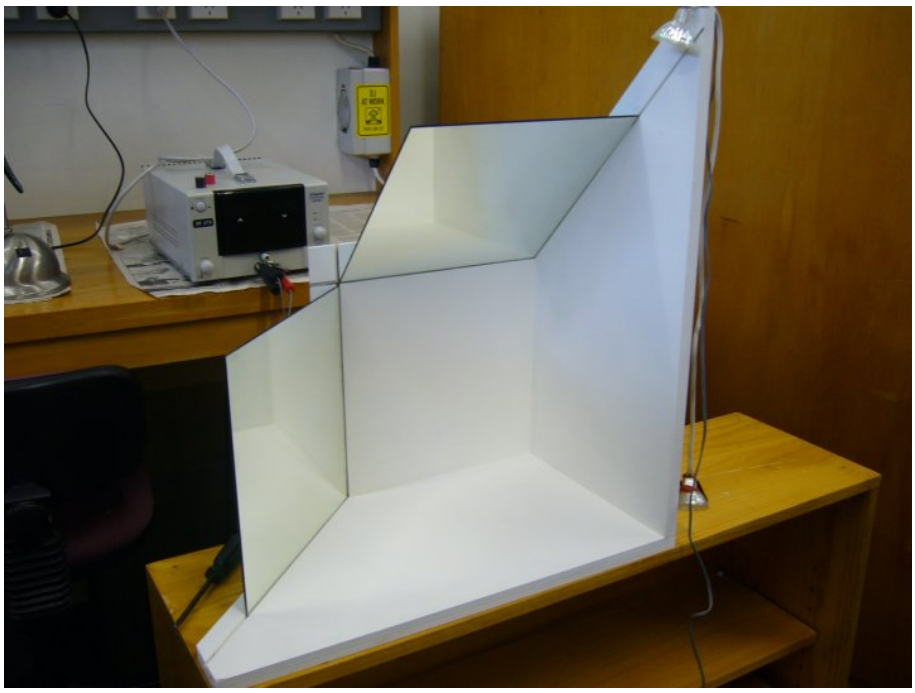

Figure 4.8: The mirror box frame designed to provide an extra two scene views using a single camera.

positions.

When the calibration process was finally made to function in a correct manner, it was still found that 3D measurements taken from the scene contained considerably more error than the initial tests using two separate stationary cameras. For this reason it was concluded that while the concept and accuracy possible with a stereo vision setup has been demonstrated, with the initial test software and stationary cameras, the use of a single camera and mirror for reducing the number of required video devices was probably not a viable solution. This was decided mainly because because of the added error in 3D measurements, which was attributed to the huge decrease in individual view image size and therefore spacial resolution. The views themselves were 29.6% and 23.0% of the total image . Not only does this decrease in spacial resolution directly effect the reconstruction due to point position errors, but it would also introduce a large amount of error into the initial camera calibration process, therefore producing error in the intrinsic and extrinsic camera parameters used during reconstruction. Included in Figure 4.9 is a Matlab plot depicting some the results gained while calibrating for two effective camera views, using a single physical camera and a mirror.

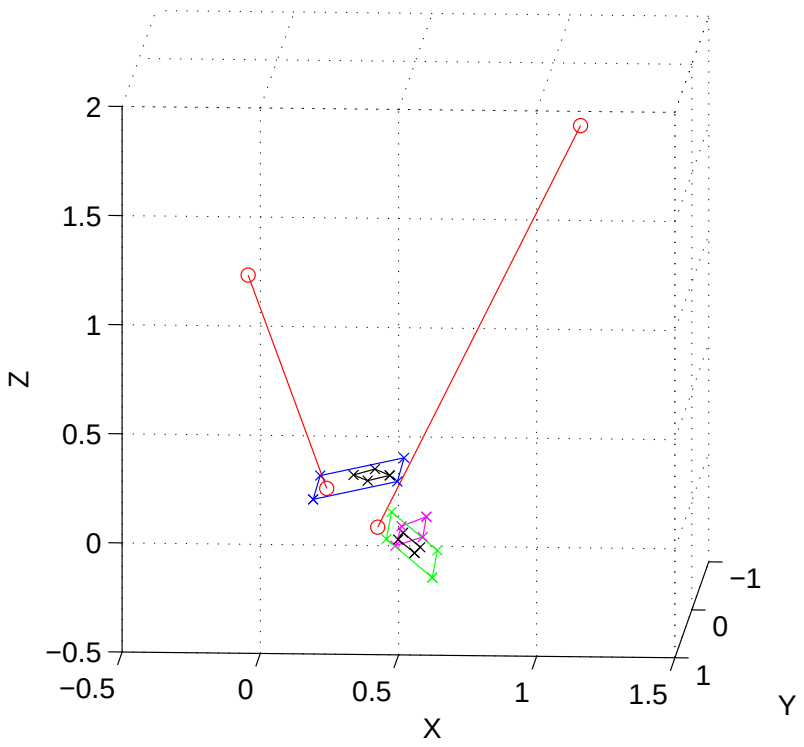

Figure 4.9: A plot in the world reference frame of points resulting from the use a mirror to produce two effective camera views of a checker board scene as taken by single physical camera. The plot is viewed from a downwards direction. In red are the optical centers, optical axis and principal points each camera. Shown in blue and green are the normalised camera reference frames of each of the cameras. Plotted in black are four image points in each image, corresponding to the outer corners of a checker board calibration pattern. Shown in pink are the reconstructed 3D points corresponding to the four checker board points in each image.

The information presented in Figure 4.9 if fairly difficult to interpret at first glance, however after studying the image for some time it can be seen that the reconstructed outer checker board corners from the two image views do indeed outline a rectangle, when projected into the 3D world reference frame. It was also confirmed, by examining and rotating the plot in Matlab, that the four points lay in a single plane, as would be expected. These are two very promising results, especially because they confirm that the camera calibration has indeed worked to some extent. When the 3D positions of the four checker board corners were used to reconstruct the four checker board edge lengths, the results were less promising. The checker board used for the calibration of the mirror setup was a 10×8 checker board with 20 mm squares. The four reconstructed corners

should define a 180 mm × 140 mm rectangle. The results of reconstructing the checker board edge lengths are included in Table 4.2.

Object Measured	Calculated Length	Actual Length	Error
Top Checker Board Width	100 mm	140 mm	28.57%
Bottom Checker Board Width	106 mm	140 mm	24.29%
Left Checker Board Height	190 mm	180 mm	5.56%
Right Checker Board Height	181 mm	180 mm	0.56%

Table 4.2: Stereo reconstructed distances compared to actual physical distances. As reconstructed from camera parameters using a mirror to create two effective camera views with a single physical camera.

On examining the measurements in Table 4.2 it is quickly realised that there is an unacceptably large error in the checker board width measurements. There is also error in the height measurements, although they are suprisingly much smaller than those assosiated with the width measurements. Overall the error in the measurements still means that this particular setup would not have been very useful for the small distances involved in insect research, and as a result methods of reducing this error should be investigated.

As mentioned earlier the error in the reconstruction was largely attributed to a reduced spacial resolution effecting both the calibration and reconstruction processes. Therefore the obvious method of reducing this error would be to increase the spacial resolution of the view images. This can be achieved in a number of ways, the most obvious of which is to use an additional camera instead of the mirror setup. However, there are other solutions to the problem, these include; using imaging devices with a greater image resolution, reconfiguring the physical mirror box setup so that there is less wasted space in the image, or even using camera zoom to ensure that the area to be measured occupys the majority of the camera frame.

After reviewing the problems and possible solutions it was concluded that implementation of the system software would continue using the single camera currently available. This decision was made because resources were not available for further imaging devices or the production of a new mirror setup. This ultimately means that the software will need to be tested again while implementing some of the proposed methods for reducing reconstruction errors. In particular it would be interesting use at least one other video camera, although it would also be interesting to investigate the proposed three camera setup. However, due to research time constraints these possibilities would be set aside as

possible future work.

The next step in the creation of the movement measurement system was to implement software to determine a solution to the stereo correspondence problem. This problem was introduced, with methods of reducing the correspondence problem solution space, in Section 2.3.2.

Due to the relatively large base lines involved in the proposed stereo setup thus far it was decided that there was a high chance that correlation techniques would produce significant errors in their assumptions. This, combined with the similarity between individual markers to be used in the proposed feature tracking system, would mean that correlation techniques are not well suited to this application. For these reasons implementation focused on the epipolar geometry method for reducing the correspondence problem solution space. To this end software was written to calculate; the fundamental matrix transform between the image from a given calibrated camera to the image of another, as well as the epipoles in each camera image space. Using this information, image points in one image can be transformed into their corresponding epipolar line in the other image. The feature points in the second image can then be checked to find the point closest to the epipolar line, which should be the correct solution to the correspondence problem.

Testing of the correspondence problem solution software proved to be very difficult due to the errors introduced at the camera calibration stage. For this reason the correspondence problem solution software will need to be tested more conclusively with the acquisition of additional video imaging hardware.

At this point it is worth noting that the problem of point occlusion between images has not been dealt with in the software to date. As mentioned earlier, it has been proposed that one way of reducing the effect of point occlusion is to use a third scene view in an attempt to increase the chances that a given point is viewable from at least two cameras.

As an overview of the stereo vision reconstruction and correspondence problem code a pseudo-code listing has been included in Algorithm 2. The listing outlines the major steps in the stereo vision software.

Algorithm 2 Stereo Reconstruction

```
for each View of scene do
  call Blob Detection algorithm to get Blob List
end for
for each Blob List "List A" do
  for each Blob "Blob A" in "List A" do
    for each other Blob List "List B" do
      Calculate Epiline of "A"
      Find Blob "B" in "List B" closest to Epiline of "A"
      Reconstruct 3D Position from "A" and "B"
      new Tracker Point(3D Position)
      Add Tracker Point to Point List
    end for
  end for
end for
return Point List
```

4.4 Tracking

In order to make measurements of a moving insect it is useful to be able to keep track of the located insect markers and track them between image frames in a video, as this allows the movement between frames to be determined rather than just recording the positions of two seemingly unrelated markers. For this reason a simple tracking system was developed after reviewing literature on the subject [37, 38, 39].

It was decided that the tracking system would be kept simple so that more time could be spent on the development of the other insect measurement systems. As such, the tracking system was implemented as a simple first order linear extrapolation tracker. This tracker operates by using the past velocity and direction of a point to define an area where the point should be located in the next frame, the algoriothm implements a nearest neighbour search to find the point closes to the center of the search area. Essentially, a tracking system of this type operates on the assumption that the time step between frames is small enough to ensure that the momentum of the object will not have changed a significant amount due to inertial effects. In practice trackers of this sort are not particularly robust, but can often still perform adequate tracking in many instances.

In order to define the search area, a distance threshold was defined in the software. This threshold was used to restrict the search for matching points in the next frame. When new

points are added to the tracked point list they are assigned a zero 3D velocity, this means that when the next frame is processed the algorithm will effectively conduct a nearest neighbour search with the points previous position, as the search region is centered on the old position. Once a match is found to the tracked point then a velocity is calculated from the previous and current frame positions. This velocity is in turn used in the next frame to move the defined search radius to a more appropriate center. An image showing an example of the tracking systems operation in over three artificial 2D frames is presented in Figure 4.10, the concept presented within this diagram can be directly extended into 3D space as in the operation of the actual tracker.

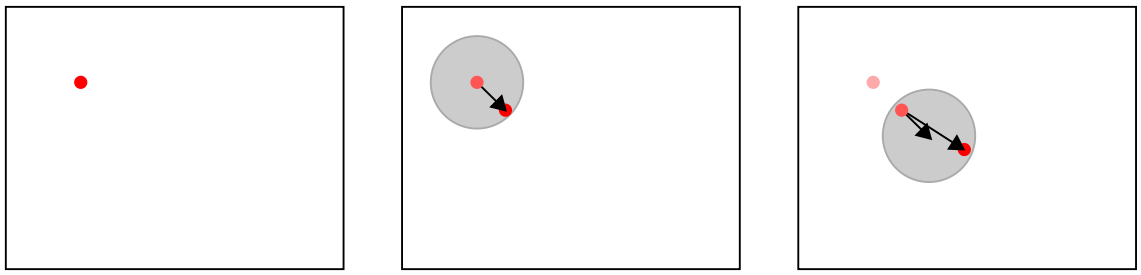

Figure 4.10: Three artificial frames depicting the operation of the designed tracking system. Left: A frame containing a newly found feature point. Middle: A frame showing the old image point (as a faded dots), the search area around this point and the point found nearest to the center of the search area. Also depicted in the calculated velocity vector between the old and new positions. Right: A frame showing old points (as a faded dot), the velocity vector used to locate the center of new search area, the closest point to this center within the search area, and the newly calculated velocity vector.

From this description the reasons why this sort of tracker system is not particularly robust should be fairly clear. Firstly, given multiple points that are detected in a similar area in a given frame, the algorithms simple nearest neighbour approach can easily get confused between the two objects. Secondly, given an object that is already moving with a velocity greater than the defined search radius when it is detected, the algorithm will lose this object in the next frame, as it will have passed beyond the search radius. This will result in the algorithm losing the point and recognising it as a newly found point in the next frame.

The tracking system was tested by processing a short video sequence containing small swinging markers. During this testing it was found that the system performed well in the

basic tracking task and it was concluded that the overall performance of the system was adequate for the requirements of this research.

A pseudo-code overview of the tracking system and how the associated software progresses is included in Algorithm 3.

Algorithm 3 Tracking

```
for each Tracked Point in Tracked List do
  Calculate Estimated Position of Tracked Point with its Velocity.
  for each Point in current frames Point List do
    Find Distance from Point to Estimated Position
    if Distance is within Search Range then
      if Point is closest found to Estimate Position then
        Keep Point as Found Point
      end if
    end if
  end for
  if Found Point then
    Calculate Velocity from Tracked Point to Found Point
    Remove Found Point from frames Point List
    Replace Tracked Point with Found Point in Tracked List
  else
    Remove Tracked Point from Tracked List
  end if
end for
Set remaining Points in frames Point List to have zero Velocity
Add remaining Points in frames Point List to Tracked List
```

4.5 Structure, Pose and Records

A feature that would be very useful in future iterations of the movement measurement and tracking is the ability to collate the located marker positions with the actual pose of the insect being tracked. As such a result into methods of detecting pose or assigning feature points to the subjects body parts should be investigated.

A fairly rudimentary method of achieving this structure and pose recognition has been proposed by this researcher. This method would use a description of the insect structure to perform an exhaustive search across the located feature points and select the best match allocation between feature points and the defined structure. In theory this matching

process would be fairly robust as the exoskeleton structure of many insects means that the outer boundaries of the animal are fairly ridgid, as opposed to mammals and the like who have flexible and therefore less structured tissue as their outer layer.

The current proposition is that the application would load a defined insect structure from an extensible markup language (XML) file. This XML file would contain the relations between the marker points placed on the insect for tracking. In particular, such relationships could include; the distance between points and ranges within which they might vary, ranges of angles defined between sets of three points and sets of co-linear points.

Once the points in the structure have been allocated to associated tracked point positions the application could also be made to redraw the wire frame structure of the insect so that this could be quickly visually compared with the actual visual images being processed, in order to problems in the detection and tracking.

The final step in the movement measurement process is to record the measurements taken. The easiest way for this to be done if for the various tracked point positions to be exported as individual columns in a simple spread sheet. In this method rows would correspond to successive time steps with blank or zero values would be inserted for entries when a point has not been found yet, or has been lost.

A slightly more complex means of recording the data would be to pair this recording system with the structure recognition system. In this way the output from the measurement system could be made much more useful. The system could then not only record the values of located points, but also which structural element these measurements are associated with in the attached structure definition XML file. Also, points lost points or points not allocated by the structure correspondence could be output separately so that they may be checked by a human researcher. In this way a researcher might be able to better identify any missing correspondence or whether a point is simply noise.

Chapter 5

WETA Application

As stated in Section 2.4, one of the goals of this research was to begin the development of an application which will provide a link between the force and movement measurement systems. Initially it is intended that this application facilitate further investigation into object detection and tracking using CV techniques. Eventually the application will instead provide an easy to use interface that reduces the complexity involved in using the measurement systems.

This section contains a brief documentation of the current state of the GUI application, which has been named Weta Evaluation, Tracking and Analysis (WETA). Section 5.1 contains a short introduction to the two major open source libraries used in the creation of WETA. Following this library introduction is Section 5.2, which deals with the current visual layout of the GUI. Finally, Section 5.3 deals with the software structure behind WETA, in particular the callback structure and modularity of the design, which should allow WETA to be used as a foundation for further investigation into feature detection, and eventually object tracking.

It is worth noting that WETA has not yet reached the point of reducing the complexity presented to users. This is because the application is still being used to investigate the use of different CV techniques. This has ment a large array of controls have been included to allow fine tuning and testing of the different algorithms. It is intended that these will be removed at a later stage.

5.1 Foundation Libraries

There were two major open source libraries used in the development of WETA. These are the GIMP Toolkit (GKT+) 2.0 and Intel's Open source Computer Vision library (OpenCV). This section gives a brief introduction to these two libraries and why they were used.

GTK+ was originally developed for the GNU Image Manipulation Program (GIMP), hence the name GTK+, and is released under the GNU Lesser General Public License (LGPL). The toolkit is actually a collection of libraries that can be used together to produce GUIs. The original libraries used by GTK+ were the G library (GLib) and GTK+ Drawing Kit (GDK), these have since been added to to allow for better text rendering and interface accessibility by adding the Pango and the Accessibility Toolkit (ATK) libraries [40].

The major reason for choosing GTK+ 2.0 as the major library for creating the WETA GUI was the desire to use an open source desktop graphics library. From this point the decision to choose GTK+, as opposed to one of the multitude of other similar open source desktop graphics libraries, was a fairly arbitrary decision made largely because of the developers desire to familiarise themself with the GTK application programing interface (API).

OpenCV is an open source CV library originally developed by Intel. OpenCV was release by Intel under a BSD license, and is free for commercial and research use. The library was apparently build with a focus on real time processing, and in order to aid this goal Intel optimised many routines to make use of their Integrated Performance Primitives (IPP).

The OpenCV library is comprised of four main parts, these are; CxCore, CvReference, CvAux and HighGui. CxCore contains the major data structures and the initialisation functions associated with the library, CvReference is largely a collection of common CV algorithms and transformations, CvAux is contains CV algorithms which rare more complex and often use the more common algorithms, and finally HighGui is a basic library for implementing GUIs for presenting CV applications created with OpenCV. In WETA the GTK+ library served to perform much of the functionality usually associated with HighGui, this was done because GTK+ is more complex and allowed for better program

structure and versatility.

OpenCV was chosen as the foundation CV library used in WETA mainly because it was open source and because of the wide variety of computer vision algorithms and techniques it makes available. Developers realised early in the undertaken research, that it would not be a viable option to develop all of these techniques independantly and that by using OpenCV a more thorough investigation of CV techniques would be possible in the available time span.

In recent years OpenCV has been used in the development of very large number of CV applications. Some of these include work on human-computer interation, automation of robotics and even biological classification [41, 42, 43]. A brief introductory overview of some other applications that are possible using OpenCV is contained in work by Cavallaro [44]. More information on OpenCV can be found at the OpenCV Library Wiki [45].

5.2 Visual Layout

This section introduced the visual layout of the WETA GUI. The GUI layout was designed using the Glade Interface Designer (Glade), Figure 5.1 shows the GUI layout at the end of the conducted research and development process.

The WETA GUI consists of three major parts, these are; the video area, plot area, and controls. The video area is located at the top left corner of the GUI and consists of an area for the display of video input and the controls associated with this display. The plot area just below the video area, is the area where measured force data collected from the proposed force sensitive surface will eventually be displayed. The Control area is located along the right hand edge of the GUI and contains the various controls associated with the features of the application. At this point these controls include; controls for multiple view definition in a single video input, view calibration controls and feature point search controls.

It is intended that the majority of the controls will eventually be removed from the front GUI layout. This is largely because the inclusion of these control on the front screen increases the percieved complexity of the application. By later removing controls associated with testing and hiding the other controls, so that they can be accessed via

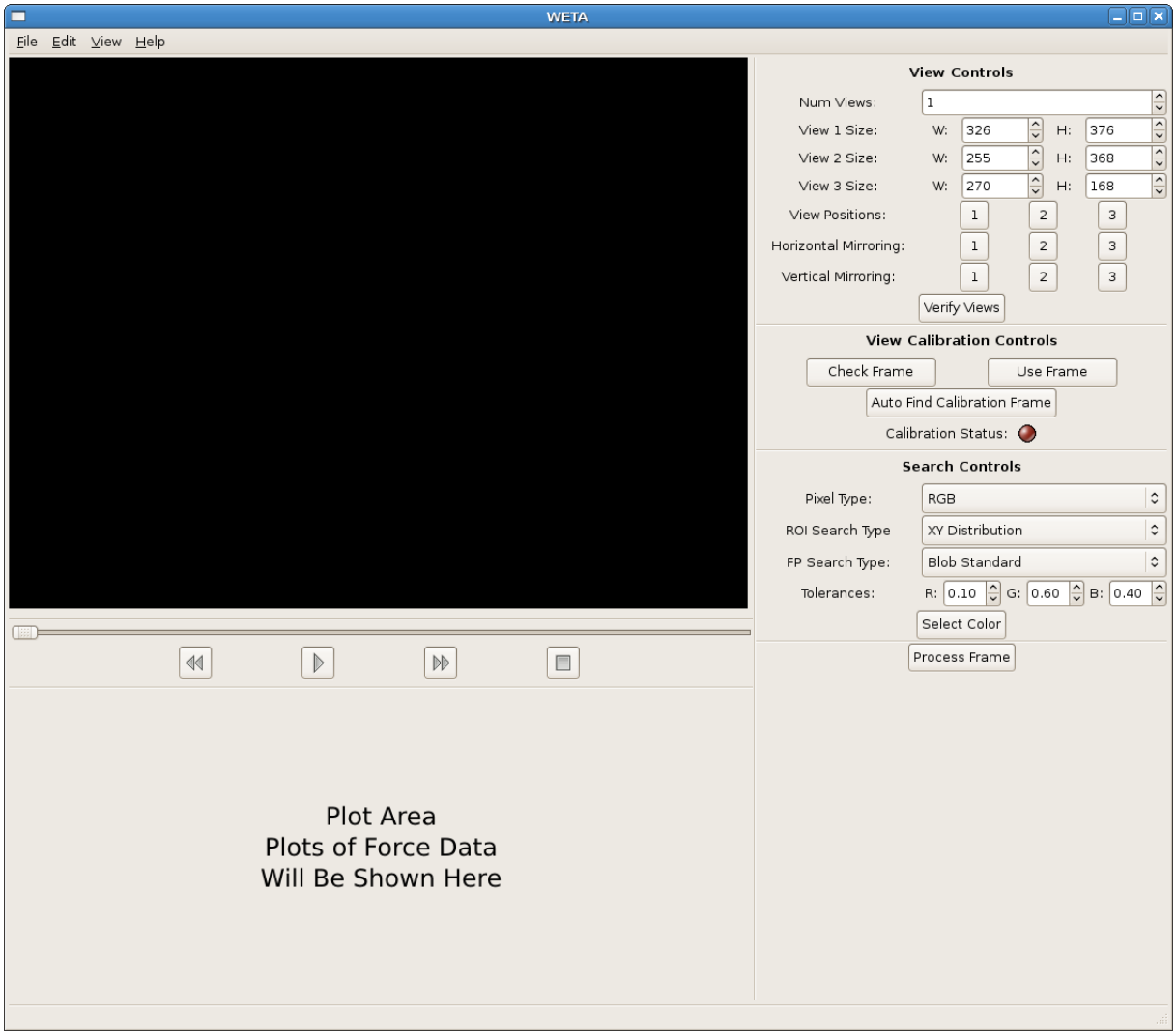

Figure 5.1: A screenshot showing the layout of the WETA GUI application.

the drop down menu system if needed, the percieved complexity of the application will be greatly reduced.

5.3 Software Structure

The structure of WETA is largely dependend on the GUI layout produced with Glade. This is typical of many of applications that require user interaction, as the information provided by the user by interacting with the GUI needs to be marshalled into the

background software. This marshalling of user input is done by the callback handler `WetaCallbackHandler`. This is shown in Figure 5.2, which contains a block diagram of the basic software structure. The majority of the interaction goes to the control handler, `WetaControls`, which saves the state of all GUI controls for easy access from further parts of the application.

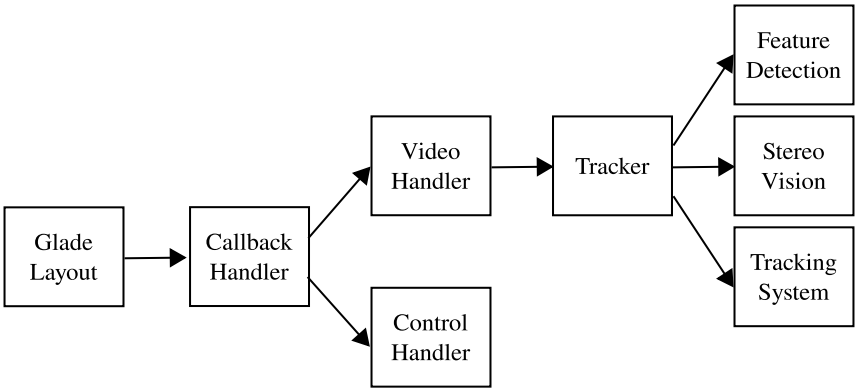

Figure 5.2: A block diagram showing the simplified software structure.

The other portion of the input marshalling is between the callback handler and the video handler, `WetaVideoHandler`, and involves the marshallng of input signals associated with progressing and stopping video processing. The callback handler also deals with ensuring that the video handler periodicly updates the output video frame when the play button is pressed.

During play, the video handler deals with retrieving video frames, passing them on for processing tasks, segmenting the image scene views when using mirrors, and also deals with any additional output that is added to the video frame before it is displayed. The video handler uses the tracker object, `WetaTracker`, to perform the majority of CV processing on the frame.

The tracker deals with sending segmented frames to the feature detection algorithm to extract features. This extraction is then followed by epipolar geometry calculations to solve the stereo correspondance problem and the calculation of 3D point positions. Finally the tracker deals with the final tracking of reconstructed 3D points. The tracker also deals with the selection of feature detection method through its coupling with the `FeaturePoint` object and its derived children.

The coupling between the `WetaTracker` and `FeaturePoint` objects has been designed to allow the investigation of further feature detection algorithms, this was designed in this way so that future work could include the investigation of a more robust detection system. It is envisaged that eventually a tracker could be designed that will remove the required user interaction of adding markers to the subject insect.

Currently there is only one feature tracking system implemented within the software. It is proposed that in future work the software that implements and calls the tracking system should be modified to produce a similar system to that of feature detection, where alternative tracking systems could be easily integrated and selected for testing. At this point the tracking system is implemented within a function of the `WetaTracker` object.

Chapter 6

Conclusion

This document has detailed research undertaken with the intention of developing a foundation for future biomimetic research at the University of Canterbury. The research has discussed biomimetics and presented a short overview of research of this sort that is being conducted in the acedemic world. In reviewing this research a number of areas were identified, where the research could possibly be improved. In particular these involved improving force measurement techniques to increase their specificity, and automating movement measurement techniques. As a result of identifying these areas, these two subjects were chosen as the main targets of investigation for this research. This resulted in an investigation being conducted into equipment and techniques that could be used in developing both the force and movement measurement systems.

The investigation into force measurement found that there were no readily available force sensors that would be suitable for insect research, and as a result a new force sensor prototype would need to be developed. Furthermore, it was decided that the best electronics components for developing such a force sensor would be piezo-electric bimorph elements. Using these piezo-electric bimorph elements, a prototype force sensor was designed and constructed.

Initially there were two candidate methods for producing force measurements from piezo-electric elements. However, after conducting some tests on individual piezo-electric elements and then repeating similar tests on the constructed sensor, it was decided that the passive or DC-coupled measurement methods would be used. This decision was made

because mechanical coupling between the elements in the prototype sensor construction was adversely effecting the active or AC-coupled measurement method.

Further testing of the piezo-electric bimorph elements and the constructed prototype sensor showed that by integrating the voltage DC-coupled signal produced by the piezo-electric elements, a measure of force excerted on them was produced. The sensor was connected to digital sampling equipment to more fully investigate its operation. During this characterisation it was found that the prototype sensor provided an adequate measures of force excerted in the two horizontal linear DOFs. Further tests carried out to investigate the prototype's sensitivity to forces in the vertical linear DOF showed that the sensor was not adequate in measuring forces in the vertical direction.

These tests on the prototype sensor lead to the development and presentation of two new sensor designs. It is intended that these further implementations will allow for additional DOFs to be measured by the sensor.

While conducting the investigation into movement measurement methods, it was concluded that the best method of measuring the 3D position of insect body parts would be with a CV system. Further research into CV techniques lead to the conclusion that stereo vision techniques would be used to reconstruct 3D positions. To reduce the complexity of the CV system it was decided that blob markers would be placed on the subject insect, and the positions of these markers would be measured and used as an indication of the insect position.

The measurement system was initially designed and implemented as three seperate systems. These were the; blob feature detection, stereo vision and tracking. These three systems were then combined into a single system.

A number of different methods were investigated during the implementation of the blob feature detection system. The most notable of these was the use of transformed colour spaces when detecting coloured blobs. It was found that the detection of a coloured object was more robust against changes in object illumination when thresholding was performed in the HSL or HSV colour space, rather than RGB. Overall it was concluded that the blob detection algorithm was not particularly robust, but was adequate for the requirements of the system.

Implementation of the stereo system, using two stationary cameras, showed that the

stereo system was indeed a good solution for measuring the 3D positions of objects. Testing of this system produced a maximum error of 1.71%, when measuring the lengths of a number of scene objects using stereo reconstruction. The system was then tested with one camera and a mirror, to produce a second scene view with a single camera. Unfortunately, using the mirror in this way significantly increased the error produced in measurements, with errors of up to 28.57% recorded. This was attributed to the decrease in spatial resolution produced when segmenting the single camera frame into two scene views.

The tracking system was implemented as a first order linear extrapolation tracker. As a result of the simple tracking algorithm implemented in the tracker, the system is not particularly robust. As such, a few of the disadvantages of this tracker were illustrated. However, the tracker was found to operate adequately for the purposes of this research. This was concluded after testing the tracker using a test video containing swinging marker objects.

Finally the components of the movement measurement system were combined and integrated into a GUI application called WETA. This GUI application provides controls for the movement measurement system components and is intended to reduce the complexity of using the system. However, the application is not currently at this desired final point in development. This is largely because at this time it is more useful as a development platform, upon which further investigation into feature detection and object tracking can be performed.

This document has presented research and development that has lead to the production of a prototype force sensor and movement measurement system indended for biomimetic research on insects. It has been found through testing of these systems that the underlining concepts behind these two measurement systems are a valid solution to the presented measurement problems. As a result a number of areas of future development have been identified to refine the produced systems.

6.1 Future Development

Throughout this document there have been a number of proposals made for future development of the measurement systems and GUI application. This section is intended as a concluding summary of those proposals.

During the development of the force sensor prototype as documented in Chapter 3, there were a number of improvements that were presented as possible future work. Of these the one of the most important improvements would be the implementation of advanced sensor designs to allow for force sensing in further DOFs. This task will in turn be coupled very closely with the miniturisation of the force sensor prototype, through the use of MEMS techniques. Once this has been done a significant amount of testing will need to be conducted to ensure that the new design works adequately.

Another item of future development identified for the force measurement system, is the reduction of sensor noise through the design of a new amplifier and other hardware. Overall, there are few problems anticipated with respec to this area of development, as this design task should be relatively simple when compared to other force sensor design tasks.

The final item of future development identified for the force sensor system is to combine multiple force sensors to form a miltiple element force sensing plate. This is the final goal of this branch of research and will require significant research and development. In particlar the future investigations should involve the design and implementation of hardware what will reduce the computational complexity involved with integrating multiple sensor outputs, and will also need to solve the problem of multiplexing the large number of piezo-electric element signals associated with a force plate.

Future development of the movement measurement system will be comprised largely of refining the systems already produced and presented in Chapter 4. In particular the major goal of future work on the movement system will be to reduce the user input required for the internal CV systems to operate and to make the systems more robust in their respective tasks. This would involve further investigations into; feature point detection, detection of the insect subject in general, improved tracking systems and the recognition of insect structure and pose.

The overall goal would be to totally remove the user input required for the detection and tracking systems to operate, although this is a difficult goal to achieve. Overall this means that some comprimise will have to be made between system internal complexity and the amount of user input, as user input usually reduces the systems internal complexity.

Chapter 4 also identified a number of areas where further work is required on the stereo vision and 3D point reconstruction systems. This further work consists mainly of improvements to the optical systems in order to improve the erros associated with the stereo vision calibration and 3D point reconstructions. These improvements would include investigations into; additional and improved imaging devices and improvement of the experimental setup.

The final portion of future development identified within this document was with respect to the developed GUI. As mentioned in Chapter 5, there is still considerable work to be done on the overall GUI and associated algorithms. It is intended that much of this work will be coupled with the development of the components of the movement measurement system, as the GUI currently provides a good platform for further development of these components. With the development of the CV systems and the desired reduction of required user input, there will be an associated reduction in complexity associated with using the GUI.

References

[1] T. Young, "The Pavek Biography - Dr. Otto H. Schmitt." Pavek Museum of Broadcasting Newsletter, August 2004.

[2] R. J. Full and D. E. Koditschek, "Templates and anchors: Neuromechanical hypothesis of legged locomotion on land," *Journal of Experimental Biology*, vol. 202, pp. 3325–3332, November 1999.

[3] R. Altendorfer, U. Saranli, H. Komsuoglu, D. E. Koditschek, H. B. Brown, M. Buehler, N. Moore, D. McMordie, and R. J. Full, "Evidence for spring loaded inverted pendulum running in a hexapod robot," in *Experimental Robotics VII* (D. Rus and S. Singh, eds.), pp. 291–302, Springer-Verlag, 2001.

[4] R. J. Full and A. Biewener, *Biomechanics: Structures and Systems A Practical Approach*, ch. Force platform and kinematic analysis, pp. 45–73. IRL at Oxford University Press, 1992.

[5] R. J. Full and M. S. Tu, "Mechanics of six-legged runners," *Journal of Experimental Biology*, vol. 148, pp. 129–146, 1990.

[6] R. J. Full and M. S. Tu, "Mechanics of a rapic running insect: Two-, four- and six-legged locomotion," *Journal of Experimental Biology*, vol. 156, pp. 215–231, 1991.

[7] R. J. Full, R. Blickhan, and L. H. Ting, "Leg design in hexapedal runners," *Journal of Experimental Biology*, vol. 158, pp. 369–390, 1991.

[8] R. J. Full, R. Kram, and B. Wong, "Three-dimensional kinematics and limb kinetic energy of running cockroaches," *Journal of Experimental Biology*, vol. 200, pp. 1919–1929, April 1997.

[9] R. J. Full and A. N. Ahn, "Static forces and moments generated in the insect leg: Comparison of a three-dimensional musculo-skeletal computer model with experimental measurements," *Journal of Experimental Biology*, vol. 198, pp. 1285–1298, February 1995.

[10] R. J. Full and D. M. Dudek, "Passive machanical properties of legs from running insects," *Journal of Experimental Biology*, pp. 1502–1515, February 2006.

[11] R. J. Full, J. E. Clark, J. G. Cham, S. A. Bailey, E. M. Froehlich, P. K. Nahata, and M. R. Cutkosky, "Biomimetic design and fabrication of a hexapedal running robot," in *Proceedings ICRA 2001*, pp. 3643–3649, IEEE, 2001.

[12] Poly-PEDAL, "Biological inspiration from the poly-pedal laboratory." Accessed Online: Oct 14th 2007 http://polypedal.berkeley.edu/twiki/bin/view/PolyPEDAL/AboutRobotics.

[13] D. Hess and A. Büschges, "Sensorimotor pathways involved in interjoint reflex action of an insect leg," *Journal of Neurobiology*, vol. 33, no. 7, pp. 891–913, 1997.

[14] J. Schmitz, "Load-compensating reactions in the proximal leg joints of stick insects during standing and walking," *J Exp Biol*, vol. 183, no. 1, pp. 15–33, 1993.

[15] J. Schmitz, T. Akay, S. Haehn, and A. Büschges, "Signals from load sensors underlie interjoint coordination during stepping movements of the stick insect leg," *Journal Neurophysiology*, vol. 92, pp. 42–51, March 2004.

[16] J. W. S. PRINGLE, "Proprioception in insects: Ii. the action of the campaniform sensilla on the legs," *Journal of Experimental Biology*, vol. 15, no. 1, pp. 114–131, 1938.

[17] L. H. Field, ed., *The Biology of Wetas, King Crickets and Their Allies*. CAB International, Oxford, 2000.

[18] A. Chand, M. B. Viani, T. E. Schaffer, and P. K. Hansma, "Microfabricated small metal cantilevers with silicon tip for atomic force microscopy," *Journal of Microelectromechanical Systems*, vol. 9, pp. 112–116, March 2000.

[19] K. Motoo, F. Arai, Y. Yamada, T. Fukuda, T. Matsuno, and H. Matsuura, "Novel force sensing using vibrating piezoelectric element," in *Proceedings ICRA 2005*, pp. 2582–2587, IEEE, April 2005.

[20] G. Y. Chen, R. J. Warmack, T. Thundat, and D. P. Allison, "Resonance response of scanning force microscopy cantilevers," *Review of Scientific Instruments*, vol. 65, pp. 2532–2537, August 1994.

[21] M. Elwenspoek and R. Wiegerink, *Microtechnology and MEMS - Mechanical Microsensors*. Springer, 2001.

[22] D. Lange, I. Brand, and H. Baltes, *Microtechnology and MEMS - CMOS Cantilever Sensor Systems - Atomic Force Microscopy and Gase Sensing Applications*. Springer, 2002.

[23] T. Itoh and T. Suga, "Scanning force microscope using a piezoelectric microcantilever," *Journal of Vacuum Science and Technology*, vol. 12, pp. 1581–1585, May 1994.

[24] Efunda, "Engineering fundamentals - beam theory." Accessed Online: 13th Oct 2007 http://www.efunda.com/formulae/solid_mechanics/beams/index.cfm.

[25] J. E. Sader, "Surface stress induced deflections of cantilever plates with applications to the atomic force microscope: Rectangular plates," *Journal of Applied Physics*, vol. 89, pp. 2911–2921, March 2001.

[26] C. S. Smith, "Piezoresistance effect in germanium and silicon," *Phys. Rev.*, vol. 94, pp. 42–49, Apr 1954.

[27] Piezocryst, "Basics - piezoelectric sensors." Accessed Online: 13th Oct 2007 http://www.piezocryst.com/piezoelectric_sensors.php.

[28] I. Piezo Systems, "Introduction to piezoelectricity." Catalogue - Application Data, 2006.

[29] Y. Sun, D. P. Potasek, D. J. Bell, S. N. Fry, and B. J. Nelson, "Drosophila flight force measurements using a MEMS micro force sensor," in *Proceedings ICEMBS*, vol. 26, pp. 2014–2017, IEEE, September 2004.

[30] E. Trucco and A. Verri, *Introductory Techniques for 3-D Computer Vision*. Prentice Hall, 1998.

[31] O. Faugeras, *Three-Dimensional Computer Vision, A Geometric Viewpoint*. The MIT Press, 1993.

[32] R. O. Duda and P. E. Hart, "Use of the hough transformation to detect lines and curves in pictures," *Commun. ACM*, vol. 15, no. 1, pp. 11–15, 1972.

[33] D. Marr and E. Hildreth, "Theory of edge detection," *Proceedings of the Royal Society of London. Series B, Biological Sciences*, vol. 207, pp. 187–217, February 1980.

[34] M. Stokes, M. Anderson, S. Chandrasekar, and R. Motta, "A standard default color space for the internet - sRGB." ICC Report by Microsoft and Hewlett-Packard, November 1996. Accessed Online: 9th Oct 2007 http://www.color.org/sRGB.xalter.

[35] J. Chung and K. Shim, "Color object tracking system for interactive entertainment applications," in *Proceedings ICASSP 2006*, vol. 5, pp. 497–500, IEEE, May 2006.

[36] N. H. Reyes and E. P. Dadios, "A fuzzy approach in color object detection," in *Proceedings ICIT 2002*, vol. 1, pp. 232–237, IEEE, December 2002.

[37] E. Polat, M. Yeasin, and R. Sharrna, "Detecting and tracking body parts of multiple people," in *Proceedings ICIP 2001*, pp. 405–508, IEEE, 2001.

[38] Y.-S. Yao and R. Chellappa, "Tracking a dynamic set of feature points," *IEEE Transactions on Image Processing*, vol. 4, pp. 1382–1395, October 1995.

[39] I. K. Sethi and R. Jain, "Finding trajectories of feature points in a monocular image sequence," *IEEE Transations On Pattern Analysis and Machine Intelligence*, vol. 9, no. 1, pp. 56–73, 1987.

[40] "Gtk+ - the gimp toolkit." Accessed Online: 14th October 2007 http://www.gtk.org/, April 2007.

[41] H. sub Yoon and S.-Y. Chi, "Cisual processing of rock, sissors, paper game for human robot interation," in *International Joint Conference SICE-ICASE 2006*, pp. 326–329, IEEE, October 2006.

[42] Q. Chen, H. Xie, and P. Woo, "Vision-based fast object recongnition and distances calculation of robots," in *Proceedings of IECON 2005*, pp. 363–368, IEEE, November 2005.

[43] T. Liu, "A quantitative zebrafish phenotyping tool for developmental biology and disease modeling [life sciences]," *Signal Processing Magazine, IEEE*, vol. 24, pp. 126–129, January 2007.

[44] A. Cavallaro, "Image analysis and computer vision for undergraduates," in *Proceedings ICASSP 2005*, vol. 5, pp. 577–580, IEEE, March 2005.

[45] "Opencv library wiki." Accessed Online: 14th Oct 2007 http://opencvlibrary.sourceforge.net/, October 2007.

Appendix A

Datasheets

A.1 Piezo-Electric Vibration Elements

This piezo ceramic bi-morph element is a versatile low power electromechanical transducer capable of converting mechanical or acoustic energy to electrical energy. When the element is stressed or subjected to vibration, the minute movement causes one layer to be under tension while the other is under compression. Since the two layers are polarised in opposite directions the opposite stresses in each layer will produce an electrical output. Applications for this device would include vibration/stress sensors, acoustic pick-up sensors and micro-positioners.

Features:

- High compliance
- Low mass
- High efficiency
- Non-magnetic
- High capacitance
- Moisture resistant

Technical Specifications

Dimensions	15 mm × 1.5 mm × 0.6 mm
Capacitance	750±170 pF
Dielectric Constant	2000
Piezo Constant (k V-m/N)	12.1
Electromechanical Coupling Factor	60
Compiance (× 10 km/N)	6.6
Maximum Stress	10-100 m
Output[1]	Vibration @ 10 μm_{p-p} = 4 V_{p-p}
Impedance	1 MΩ

1 - Actuated while clamped 5 mm from lead end in a cantilever manner.

A.2 LMC660 Operational Amplifier

August 2000

National Semiconductor

LMC660
CMOS Quad Operational Amplifier

General Description

The LMC660 CMOS Quad operational amplifier is ideal for operation from a single supply. It operates from +5V to +15V and features rail-to-rail output swing in addition to an input common-mode range that includes ground. Performance limitations that have plagued CMOS amplifiers in the past are not a problem with this design. Input V_{OS}, drift, and broadband noise as well as voltage gain into realistic loads (2 kΩ and 600Ω) are all equal to or better than widely accepted bipolar equivalents.

This chip is built with National's advanced Double-Poly Silicon-Gate CMOS process.

See the LMC662 datasheet for a dual CMOS operational amplifier with these same features.

Features

- Rail-to-rail output swing
- Specified for 2 kΩ and 600Ω loads
- High voltage gain: 126 dB
- Low input offset voltage: 3 mV
- Low offset voltage drift: 1.3 µV/°C
- Ultra low input bias current: 2 fA
- Input common-mode range includes V^-
- Operating range from +5V to +15V supply
- I_{SS} = 375 µA/amplifier; independent of V^+
- Low distortion: 0.01% at 10 kHz
- Slew rate: 1.1 V/µs
- Available in extended temperature range (−40°C to +125°C); ideal for automotive applications
- Available to Standard Military Drawing specification

Applications

- High-impedance buffer or preamplifier
- Precision current-to-voltage converter
- Long-term integrator
- Sample-and-Hold circuit
- Peak detector
- Medical instrumentation
- Industrial controls
- Automotive sensors

Connection Diagram

14-Pin DIP/SO

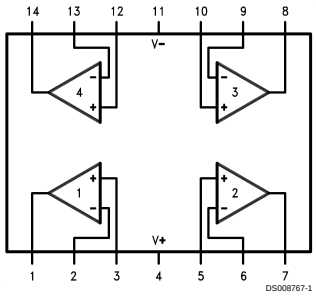

DS008767-1

LMC660 Circuit Topology (Each Amplifier)

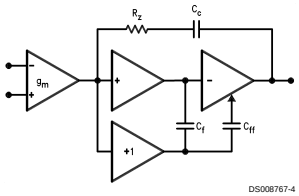

DS008767-4

Appendix B

Schematics

B.1 Power Supply

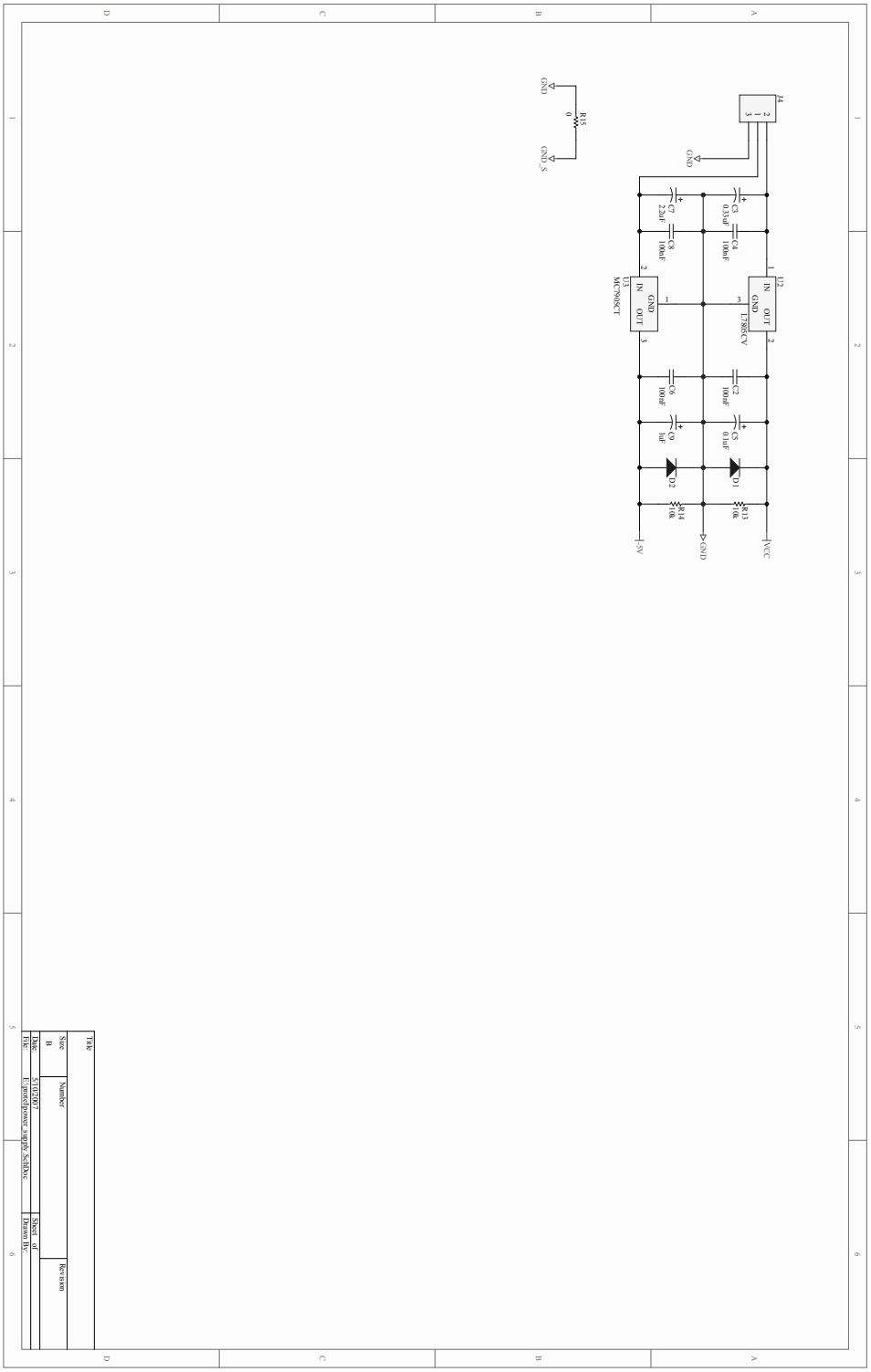

B.2 Non-Inverting Amplifier

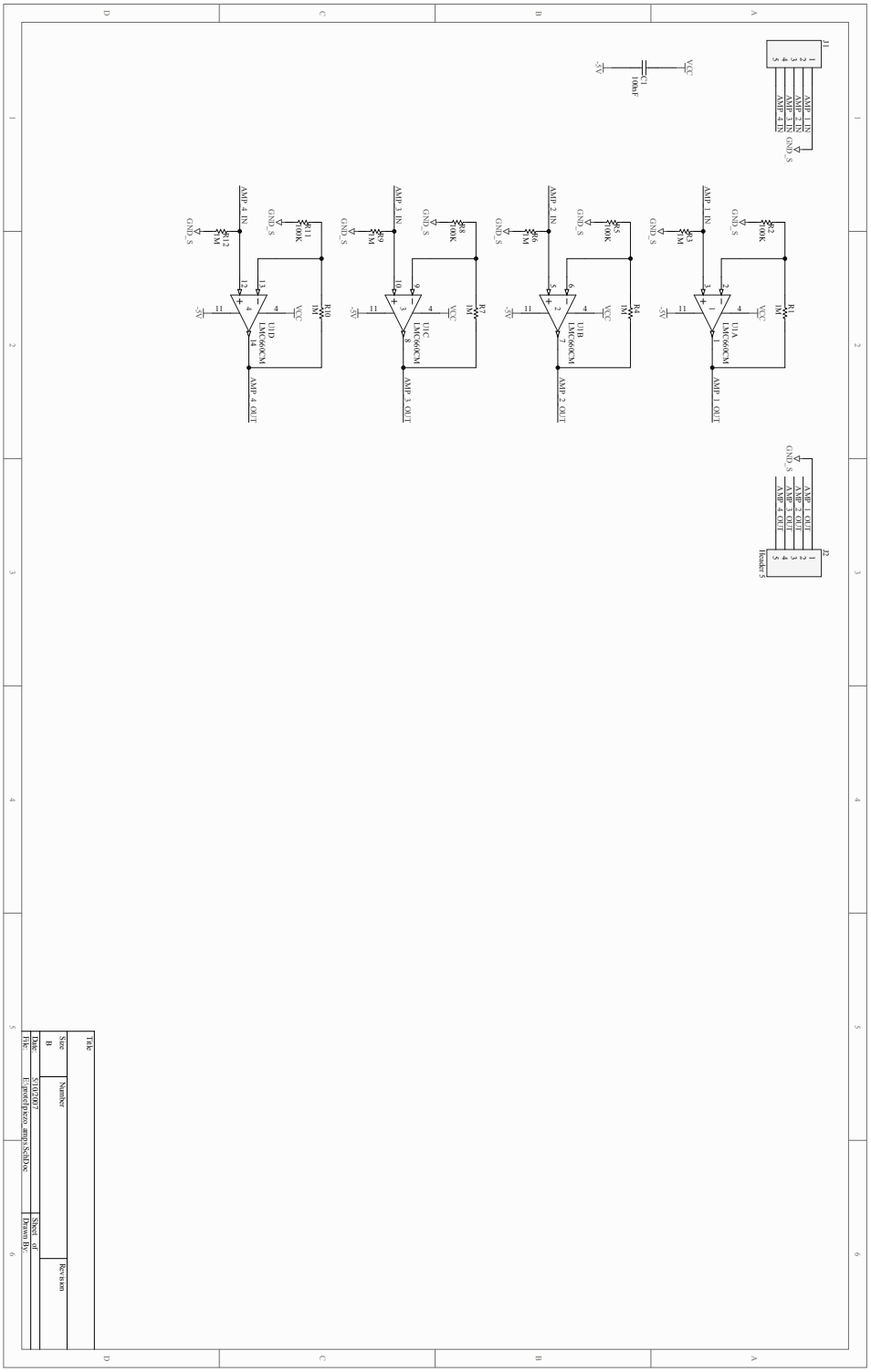

B.3 Amplifier PCB Layout